ENHANCING LOCAL ABSORPTION PATTERNS WITHIN GOLD NANO-STRUCTURES ON A DIELECTRIC SURFACE UNDER AN AFM PROBE AND WITH EVANESCENT-WAVE ILLUMINATION

by

Sina Talebi Moghaddam

B.S., Mechnical Engineering, University of Tabriz, 2009

Submitted to the Institute for Graduate Studies in
Science and Engineering in partial fulfillment of
the requirements for the degree of
Master of Science

Graduate Program in Mechanical Engineering

Boğaziçi University

2016

ENHANCING LOCAL ABSORPTION PATTERNS WITHIN GOLD NANO-STRUCTURES ON A DIELECTRIC SURFACE UNDER AN AFM PROBE AND WITH EVANESCENT-WAVE ILLUMINATION

APPROVED BY:

Assoc. Prof. Hakan Ertürk .....
(Thesis Co-supervisor)

Prof. M. Pınar Mengüç .....
(Thesis Co-supervisor)

Assoc. Prof. Hasan Bedir .....

Assist. Prof. Jeremy Mason .....

Assoc. Prof. Kürşat Şendur .....

DATE OF APPROVAL: 22.12.2015

ACKNOWLEDGEMENTS

I would like to express my deepest gratitude to my advisor, Assoc. Prof. Hakan Ertürk, for his excellent guidance, caring, providing a great research atmosphere, well-organized meetings and teaching an excellent course on radiation heat transfer, where I got introduced to this amazing field. I wish to express my sincere gratitude to my advisor, Prof. Pınar Mengüç, who taught me to think big and beyond textbooks, explaining physics of problems with simple examples, all the motivation and supported my research financially. I would also like to thank Assist. Prof. Jeremy Mason for answering my many questions and teaching an amazing course on computational material science, where I got introduced to many new ideas. I would like to thank my parents, my brother, and sister. They were always supporting me and encouraging me with best wishes. I thank my fellow lab mates for the scientific discussions and for all the fun we have had in the last two years.

This thesis has been partially supported by Center for Energy, Environment and Economy at Özyeğin University, Istanbul, Turkey.

ABSTRACT

ENHANCING LOCAL ABSORPTION PATTERNS WITHIN GOLD NANO-STRUCTURES ON A DIELECTRIC SURFACE UNDER AN AFM

This study considers enhancing localized absorption by a gold nanoparticle (NP) placed over a substrate where an atomic force microscope (AFM) tip is in close proximity of the particle. The gold NP and AFM tip are interacting with a surface evanescent wave, resulting the near-field coupling between the tip and NP and consequently enhances the absorption. This concept can be used for selective heating of NPs placed over a surface and is applicable when localized heating is desired for precise manufacturing at nanometer scales. Different tip positions are considered to identify the optimal tip location and the corresponding enhancement limits. The effects of these interactions on the absorption profiles of dielectric core-shell NPs are also studied. It is observed that using core-shell nanoparticles with a dielectric core leads to further enhancement of the absorption efficiency and a more uniform distribution of absorption over the shell. Discrete dipole approximation coupled with surface interactions (DDA-SI) employed through the study, it is vectorized to improve its computational efficiency.

ÖZET

GENLİĞİ AZALAN DALGA AYDINLATMASI İLE ATOMİK KUVVET MİKROSKOPU ALTINDAKİ DİELEKTRİK YÜZEYLERİN ÜZERİNDEKİ ALTIN NANO YAPILAR İÇİNDEKİ LOKAL SOĞURMA ALIŞKANLIKLARININ ARTTIRILMASI

Bu çalışma, atomik kuvvet mikropskopunun nano taneciğe çok yakın olarak konumlandırılan dielektrik ucu kullanılarak bir yüzey üzerine yerleştirilmiş altın nano taneciklerin üzerindeki lokalize edilmiş soğurmanın arttırılması için yöntembilimi sunmaktadır. Yüzeyde genliği azalan dalgalı altın nano parçacık ve atomik kuvvet mikroskopunun ucu ve yakın alan kenetlenmesine maruz kalmış uç ve nano parçacık plazmonik çınlamaya sebep olur. Sonuç olarak da nano parçacıklar, soğurma verimini arttırır. Bu kavram, nano parçacıkların bir yüzeyde seçilimli ve bölgesel ısıtılmasında kullanıbilir. Uygulamalı olarak ise, nanometre boyutlarındaki hassas üretimler için lokal ısıtımın gerekli olduğu durumlarda kullanılabilir. Optimal tip konumlarının ve bunlara karşılık gelen arttırıcı limitlerin tespit edilmesi adına farklı tip pozisyonları dikkate alınmalıdır. Bu çalışmada, farklı kabuk boyutlarındaki altın kabuklu ve dielektrik kabuklu çekirdek-kabuk nano-parçacıklarının kullanımının etkileri araştırıldı. Çekirdek-kabuk nano-parçacıklarının dielektrik çekirdek ile kullanımı, çekirdekteki soğurma verimini daha fazla tekdüze dağılımla artırdığı gözlendi. Kesikli çift-kutup yakınsaması ile birleştirilen yüzey etkileşimlerinin (DDA-SI) vektör haline getirilmesi, hesapsal verimi artırmak adına çalışma boyunca yapıldı.

TABLE OF CONTENTS

LIST OF FIGURES

LIST OF SYMBOLS

α	Polarization
ϵ_0	Permittivity of free space
η	Wavenumber
λ	Wavelength
θ	Incident angle
ω	Angular Velocity
$\overline{\overline{A}}$	Dipole to Dipole Interaction Matrix
$\overline{B}$	Magnetic induction
c	Speed of light in vacuum
D	Diameter of sphere
d	Lattice parameter
$\overline{E}$	Electrical field
$\overline{E}_{inc}$	Incident Electrical Field
$\overline{H}$	Magnetic field
$\overline{J}$	Electrical current density
$\overline{k}$	K-vector
k	Imaginary part of refractive index
N	Number of Dipoles
n_{bulk}	Refractive index of bulk medium
$\overline{n}$	Complex Refractive index
$\overline{P}$	Dipole Moment
$\overline{\overline{R}}$	Surface Interaction Matrix
t	Time
V	Volume

LIST OF ACRONYMS/ABBREVIATIONS

AFM	Atomic Force Microscope
ALD	Atomic Layer Deposition
AuNP	Au nanoparticle
BEM	Boundary element method
CEM	Computational electromagnetic
FDM	Finite difference method
FDTD	Finite difference time domain
FEM	Finite elements method
FIT	Finite integration technique
FVM	Finite volume method
MBE	Molecular beam epitaxy
MOM	Method of moments
NP	Nanoparticle
PDE	Partial differential equation
PSL	Polystyrene latex
SNOM	Scanning near-field optical microscope
TE	Transverse Electric
TERS	Tip-enhanced Raman spectroscopy
TIR	Total Internal Reflection
TM	Transverse Magnetic

1. INTRODUCTION

1.1. Engineering at Nano-scale

Nano-scale engineering dates back to only 1980s [1], yet its applications has already revolutionized the technology around the world. The variation of material properties for sizes visible with an optical microscope is small. However, when we enter the nano-world in which the distances are between 1-100 nanometers, the material properties can change significantly with size [2]. In nano-scale, quantum forces and effects are dominant. Properties such as phase transform points, electrical resistance, magnetic properties and thermal properties depend on the scale of the nanoparticle [2]. Nanotechnology can be used in many different scientific areas and has numerous applications in technologies important to humankind: electronic products, energy sector, manufacturing, medical engineering are some examples. Engineering at nano-scale main power lies in arranging the main structures of materials in nano-scales for achieving desired properties. It can make a material with more desirable specifications to us, for instance, lighter, tougher, more stable.

With the world's demand for energy and effects of fossil fuels on the environment, there is a considerable demand for sustainable energy. Nano-structured solar cells are more efficient and cheaper to produce and to install, which promise us a future of inexpensive solar power in every house [3]. There even considerations to design printable solar panels. With ordinary glasses windows, we can harness the heat from the sun for warming our houses in winter, however, we need mirrors instead of glasses in our windows in summer. Nano-structured enriched glasses are switch-able between glass and mirror. In chemical engineering, nanotechnology improves the efficiency of fuels production, which can use even for making high-quality fuel from low-grade raw petroleum materials [3]. Transformation of plants to ethanol, better rechargeable, and endurable batteries, and lighter materials for blades of wind turbines are some of the nanotechnology's applications in the energy sector. In medical science and biotechnology, nanotechnology applications can lead to a more transportable, cheaper,

personalized and easier to administer the product. We can have improved imaging systems for diagnostics purposes. For example, gold nanoparticles can be used for treating cancer [4] or detect early-stage of Alzheimer's disease [5]. With molecular imaging and the use of bio-sensors in nano-scale, doctors can access to a vast variety of information about their patients [6].

Two fundamental approaches of nano-manufacturing are the top-down and bottom-up approaches [7]. In the top-down approach, we reduce the size of a large material to a nano-scale size. lithographic patterning techniques is an example of top-down approach. In bottom-up approach, large sized products are manufactured from nano-sized components, such as the production of electronic device surfaces, which are water and shock resistance. It is essential to understand dominant controlling physical rules of materials in order to manipulate material in these scales. Finding the nano-scale material is also important. The nano-material usually name for the specific shape and dimension they have. A key challenge to work in these small scales is identify them and develop an understanding related to the physical behavior of matter in these sized. Both experimental or analytical methods can be developed and used for this purpose.

1.2. Plasmonics

In recent years, the optical properties of noble metal nanoparticles (NPs) have received significant fundamental and technological attention due to their radically altered physical behavior compared to bulk materials. Noble metals such as gold (Au) and silver (Ag) are well known for their resonance excitations in the visible light ranges. The optical properties of metallic nanoparticles are controlled by the oscillation frequency of free electrons on the surface of the nanoparticle. Whenever these oscillations resonate with an incident electromagnetic (EM) field, localized surface plasmonic resonance (LSPR) occurs [8–12]. The fundamental concepts in plasmonics are presented in [13], and Stockman discussed the fundamental of nano-localization of optical energy and theoretical ideas in plasmonics in [14]. Bharadwaj et al. reviewed the recent work in the field of optical antennas, which exploit the properties of metal nanostructures with coupled plasmas at optical frequencies [15].

Metallic NPs usually have improved optical absorption at LSPR wavelength. The presence of an AFM probe's tip can intensify the near-field coupling that helps localized heating at the tip of AFM and NP. The combination of these two phenomena can significantly intensify the absorption in NP. Therefore, using AFM near the resonance wavelength to heat and melt NPs locally is considered for nanofabrication [16]. In addition to applications in heating, understanding the optical properties of nanostructures in the proximity of an AFM probe can influence tip-based imaging, sensing, near-field optical microscopy (SNOM) and tip-enhanced Raman spectroscopy (TERS) [17–19].

Despite the intensified heating of metallic NPs at their resonance wavelengths, a non-plasmonic dielectric tip does not absorb the incoming radiation and simply changes the absorption efficiency of the NP at resonance wavelength. A comparison between heat absorption in metallic versus non-metallic NPs was carried out in [20,21]. Alonso-González et al. outlined the theory of NP and tip interaction, discussing how they generate near-field effect and the origin of SNOM and surface spectroscopy [22].

The behavior of objects under electromagnetic illumination can be identified by solving Maxwell's equations. Analytical solution of Maxwell's equations is only possible for a few known configurations. For arbitrarily shaped objects, numerical solution of Maxwell's equations can be carried out by computational electromagnetic methods (CEM) to predict the optical properties of a scattering particle under different boundary conditions. Semi-analytical methods such as discrete dipole approximation (DDA) can be used for solving these problems efficiently. DDA is a CEM that is capable of calculating the optical behavior of arbitrarily shaped, non-homogeneous, anisotropic objects. DDA was first introduced by DeVoe [23] and, its formulation was later on developed by Purcell and Pennypacker [24]. The main approximation considered in DDA is representing a continuous material by a number of dipoles. There are well-known open source packages for DDA such as DDSCAT, written in FORTRAN, developed by Draine and Flatau [25, 26] , and ADDA written in C, developed by Yurkin and Hoekstra [27, 28]. These packages are widely used for understanding the interaction of particles in open space with direct propagating waves.

For objects placed on a substrate, the substrate should also be approximated by dipoles that significantly increase the computational time. To prevent this, the surface interaction is instead formulated analytically in the interaction matrix. To model light scattering from particles on a semi-infinite surface, Taubenblatt and Tran [29] introduced the surface effect to their Fortran implementation. Later on DDSURF was developed by Schmehl and Nebeker [30, 31]. While these two models are not released as an open source software to the general public, an open source MATLAB^{TM} toolbox, DDA with Surface Interaction (DDA-SI), was developed by Loke and Mengüç [32]. The toolbox was verified by the authors for plane wave-particle and surface wave-particle interactions against solutions by FEM and FDTD methods. Moreover, MNPBEM, a MATLAB toolbox for the simulation of metallic NPs using the boundary element method (BEM), also showed a perfect match with DDA-SI for a single AuNP on a surface [33]. The toolbox was also validated for microwave analog experiments for the far-field scattering of non-absorbing and absorbing particles on a surface [34].

The feasibility of nano-manufacturing using AFM has been investigated experimentally by Hawes et al. [16], where 50 and 100 nm AuNP were heated by a 532 nm wavelength laser in close vicinity to a Si AFM probe. The results showed that melting or evaporation of AuNPs is possible only beyond certain thresholds in the particle-probe interaction time and also the average distance between the probe and surface and between the tip of the probe and the particle are also found to be important. For heating of Ag and Au NPs on different substrates, Huda et al. [35–37] investigated the effect of Si and Au tapping mode tip with finite element method (FEM). Their results showed that Au tip has a negative effect on the heat absorption of AuNP at the resonance wavelength. Moreover, Si tip can effectively increase the rate of absorption by the NP [37]. They also investigated the effect of particle size, tip radius and incident light polarization on Au and Ag NPs heating, and showed that transverse magnetic (TM) illumination is the more effective for maximizing absorption [35]. In another study, Loke et al. [38] investigated the effect of a tip for increasing the dipole intensity in a 20 nm AuNP . This study also confirmed that TM compared to TE incident polarization is more effective for heating AuNP and also studied optimum shaft length for having the maximum normalized dipole field intensity in the NP [36].

The current thesis focuses on identifying the optimal high-permittivity silicon (Si) tip's position in 3-D space relative to a spherical AuNP for heating on a dielectric substrate under surface evanescent illumination caused by total internal reflection. The goal is to identify patterns between heat absorption by NP and tip's spatial location and find an optimum location to move the probe in order to selectively heat AuNPs. While only the absorption patterns are presented, the patterns can be converted to localized heating rates either using macro-scale radiation transfer calculations as presented by [35–37], or by adapting near-field calculations similar to those reported by Francoeur and Mengüç [39], Didari and Mengüç [40–42], and Edalatpour et al. [43]. Alabastri et al. [9] presented a temperature dependent permittivity model to calculate the temperature effect in plasmonic systems.

Spatial Optimization in 3-D space is challenging due to the required computational resources as computation time demand for these solutions are significant. Therefore, DDA-SI is modified to improve its computational efficiency and the modified toolbox is used for the entire study.

2. Background Information

2.1. Maxwell's Equations

Maxwell's four equations constitute the fundamentals of electricity and magnetism [44]. Maxwell's first law states that the electrical field produced by an object is only determined by the amount of charge inside the object and the electrical field does not depend on the object shape or size. The second law of Maxwell states independent of an object's shape, size or charges. The number of magnetic field lines entering and exiting an object will always be exactly the same. The third law states that changing magnetic field through a loop of wire creates and electric field along the loop. Maxwell's fourth law states that the current and any changing electric field along a length of wire creates a magnetic field encircling the wire.

These are in combination written as [44]:

$$\text{Gauss's law for electricity} \qquad \nabla \cdot \overline{E} = \frac{\rho}{\epsilon_0} \tag{2.1.1a}$$

$$\text{Gauss's law for magnetism} \qquad \nabla \cdot \overline{B} = 0 \tag{2.1.1b}$$

$$\text{Faraday's law of induction} \qquad \nabla \times \overline{E} = -\frac{\partial \overline{B}}{\partial t} \tag{2.1.1c}$$

$$\text{Ampere's law} \qquad \nabla \times \overline{B} = \frac{\overline{J}}{\epsilon_0 c^2} + \frac{1}{C^2}\frac{\partial \overline{E}}{\partial t} \tag{2.1.1d}$$

where, $\overline{E}$ is the electrical field, $\overline{B}$ is the magnetic induction, ϵ_0 is the permittivity of free space, $\overline{J}$ is the electrical current density and c is the speed of light in vacuum. Some references to study the fundamentals of classical electrodynamics are [44–46].

2.2. Polarization of Electromagnetic Waves

Electrical component of a plane wave can oscillate in any direction normal to the direction of propagation. Consider a plane wave that is propagating in $x-$direction, the

electrical field can oscillate in an arbitrary direction in the $yz-$plane and the direction of oscillation determines the polarization of the plane wave. When the electrical field oscillates in $y-$direction the equation of the plane wave will be :

$$\overline{E} = E_0 \exp\big[i(\eta x - \omega t)\big]\hat{e}_y \tag{2.2.1}$$

where E_0 is the amplitude of the wave, η is the wavenumber and $\omega = \eta c$. If the wave polarization is instead in the $z-$direction:

$$\overline{E} = E_0 \exp\big[i(\eta x - \omega t)\big]\hat{e}_z \tag{2.2.2}$$

In Equations 2.2.1 and 2.2.2, the $\overline{E}$ oscillates in a straight line and the waves are linearly polarized. By combining two linearly polarized waves other types of polarizations are possible. A circularly polarized wave propagating in the $x-$direction has two linearly polarized waves with equal amplitudes along the $y-$ and $z-$axes, and one of them has a $\pi/2$ initial phase. When the tip of the electrical field tracks a circle in counter clock wise direction (right hand circular polarized), the equation is:

$$\overline{E} = E_0\big\{ \exp\big[i(\eta x - \omega t)\big]\hat{e}_y + \exp\big[i(\eta x - \omega t + \pi/2\big]\hat{e}_z\big\} \tag{2.2.3}$$

When the electric field tracks a circle in clock wise direction (left-hand circular polarized), the electrical field is:

$$\overline{E} = E_0\big\{ \exp\big[i(\eta x - \omega t)\big]\hat{e}_z + \exp\big[i(\eta x - \omega t + \pi/2\big]\hat{e}_y\big\} \tag{2.2.4}$$

In the case the y and $z-$axis components of Equations 2.2.3 and 2.2.4 are not equal, there will be a elliptically polarized wave. For an elliptically polarized wave with $\overline{E}$ tracking an ellipse in counter clock wise direction (right hand elliptically polarized) the equation is:

$$\overline{E} = E_1 \exp\big[i(\eta x - \omega t)\big]\hat{e}_y + E_2 \exp\big[i(\eta x - \omega t + \pi/2\big]\hat{e}_z \tag{2.2.5}$$

Another terminology used in literature is Transverse Electric (TE) and Transverse Magnetic (TM) polarizations. In wave-guides, the electrical or magnetic field of the wave can have components in the direction of K-vector. TM means that the E field is not transverse to the direction of propagation, but has a components in this direction. In a similar manner, TE has a magnetic component in the direction of propagation.

2.3. Snell's law

Speed of light changes with respect to the refractive index of media. This phenomena leads to a change in direction of ray of light passing through refractive media with varying indices of refraction. Consider two media with index of refraction n_1, n_2 as shown in Figure 2.1. As light passes the border between two medium, the light will refracted to a greater or lesser angle. Light is travelling from medium one to two; if $n_1 > n_2$ then the light speed with increase and the light will refracted away from the normal. On the contrary, if $n_1 < n_2$ the light will slow down which makes the light beam refract towards the normal line. The snell's law formula will be:

$$\frac{\sin\theta}{\sin\theta''} = \frac{\lambda}{\lambda''} = \frac{n_2}{n_1} \tag{2.3.1}$$

As is defined in Figure 2.1 the wavelength of incident and refracted waves are λ and λ'' respectively, and their angles from the normal are θ and θ''.

2.4. Evanescent Wave

Equation 2.3.1 does not have a real solution for every configuration of refractive indices. Suppose light is travelling from medium one to medium two as shown in Figure 2.1, with refractive indices of n_1 and n_2, and $n_1 > n_2$. Then according to Equation 2.3.1, θ'' is:

$$\theta'' = \arcsin\left(\frac{n_1}{n_2}\sin\theta\right) \tag{2.4.1}$$

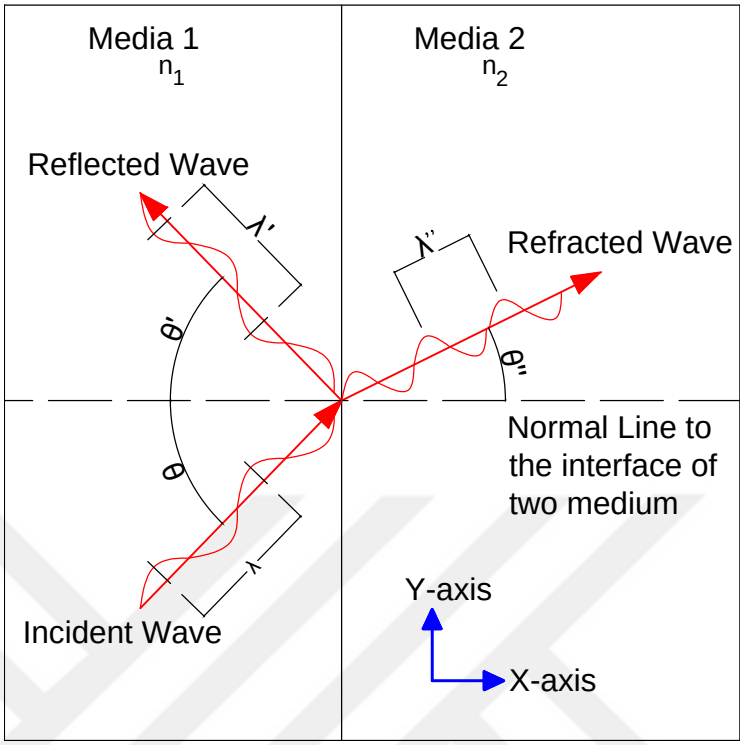

Figure 2.1: Description of Snell's Law.

For fixed refractive indexes of two medium the critical angle will be defined as the angle which Equation 2.4.1 does not have a real answer. The critical angle is:

$$\theta_c = \arcsin\left(\frac{n_2}{n_1}\right)$$

If the incident angle is larger than θ_c, there will be no propagating wave in the medium 2 and all the incident wave will be reflected into medium 1. This phenomena is called Total Internal Reflection (TIR). The wave equation in medium 2 can be written as:

$$\overline{E''} = \overline{E''_0} \exp\left[i(\overline{k''} \cdot \overline{r} - \omega t)\right] \tag{2.4.2}$$

where $\overline{k''}$ is the K-vector in the second medium. The magnitude of K-vector can be written as $|\overline{k''}| = \frac{n_2 \omega}{C}$, where ω is the angular frequency. The orthogonal decomposition

of the K-vector is:

$$\overline{k''} = k''_x \hat{e}_x + k''_y \hat{e}_y = \frac{n_2 \omega}{C} \cos\theta'' \hat{e}_x + \frac{n_2 \omega}{C} \sin\theta'' \hat{e}_y \tag{2.4.3}$$

, and considering position vector as $\overline{r} = x\hat{e}_x + y\hat{e}_y$, with combining Equation 2.4.2 and 2.4.3:

$$\overline{E''} = \overline{E''_0} \exp\left(i \frac{n_2 \omega}{C} \cos\theta'' x\right) \exp\left(i \frac{n_2 \omega}{C} \sin\theta'' y\right) \exp\left(-i\omega t\right) \tag{2.4.4}$$

The $\sin\theta''$ term in Snell's law always has a real answer. However, it may be larger than 1, when $\theta > \theta_c$, meaning that the $\cos\theta''$ in the Equation 2.4.4, will have an imaginary part:

$$\cos\theta'' = \sqrt{1 - \sin^2\theta''} = i\theta_1 \tag{2.4.5}$$

where θ_1 is a real number, combining Equation 2.4.4 and 2.4.5

$$\overline{E''} = \overline{E''_0} \exp\left(-i\omega t\right) \exp\left(i n_2 \frac{\omega}{C} \sin\theta'' y\right) \exp\left(-n_2 \frac{\omega}{C} \theta_1 x\right) \tag{2.4.6}$$

and by using Euler formula, the real part of calculated field represented by Equation 2.4.6 is:

$$Re\{\overline{E''}\} = \overline{E''_0} \cos\left(\frac{n_2 \omega}{C} \sin\theta'' y - \omega t\right) \exp\left(-n_2 \frac{\omega}{C} \theta_1 x\right) \tag{2.4.7}$$

Equation 2.4.7 show a plane wave in $y-$axis direction with an exponential decay in $x-$axis direction. This surface wave in called evanescent wave and is shown schematically in Figure 2.2.

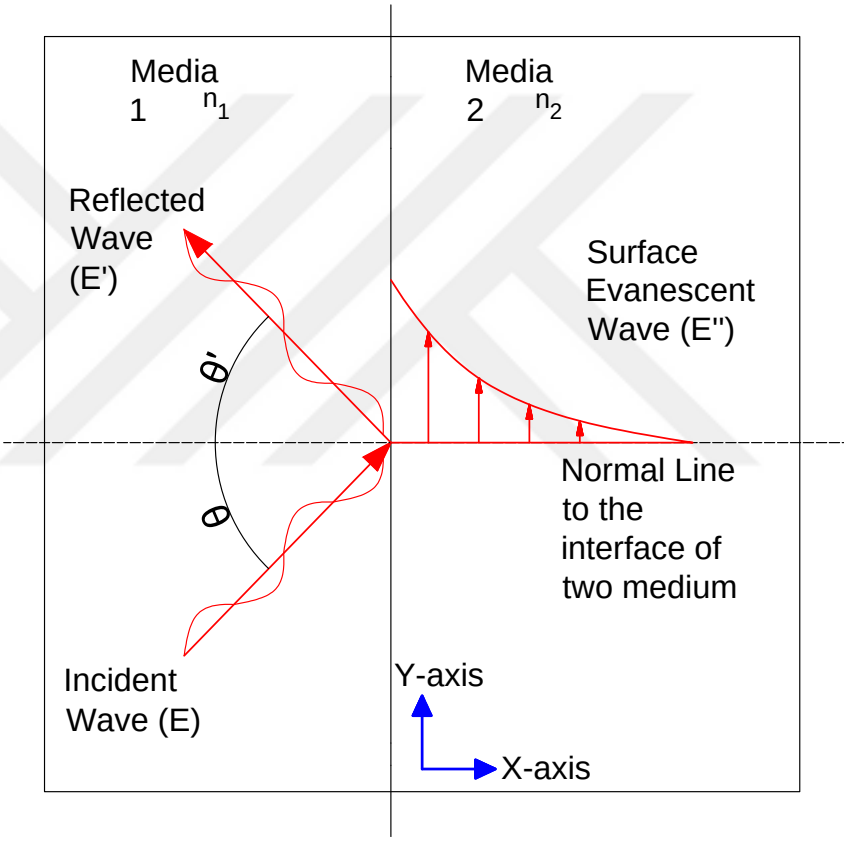

Figure 2.2: Total internal reflection generates a decaying evanescent wave on the surface.

2.5. Computational Electromagnetics

The optical properties of nanoparticles (NP) are hard and expensive to measure in experiments. The governing Maxwell equations for these particles don't have an analytical solution except for some special geometries [47]. With the use of computational electromagnetic modelling, the optical properties of NPs can be found within an acceptable range of accuracy. With these methods, we try to model the process where electromagnetic fields interact with physical objects and the environment. With computational approximations, the solution of Maxwell's equations can be used to predict all the optical properties such as scattering, absorption, extinction, far-field scattering, and near-field effects. CEM normally is used to solve electric Field ($\overline{E}$) and magnetic Field ($\overline{H}$) in the problem domain [48]. CEM models can assume symmetry depending on the problem conditions, and real world problems can simplify to spheres, cylinders or other symmetric geometrical objects. Like most of the computational methods, CEM discretizes the space domain into grids. Afterward, Maxwell's equations are solved for each point of the grid. Some well-known methods are:

- Boundary element method (BEM)

This method solves the problem in the form of integral equations, and its application is not limited for CEM as it can be used in many different areas of engineering. BEM uses integral equations as an analytical tool for the answer of the partial differential equations, then it fits the boundary values into the equations [49]. BEM is usually used for linear homogeneous media, which the Green's function of the differential equation can be calculated. For nonlinear cases, the discretization of the media is needed, which takes away the main advantage of the method. In a problem with small surface/volume ratio, BEM is often more efficient than volume methods (FEM, FDTD). However, for most problems BEM is significantly less efficient than alternatives. Metallic nanoparticle boundary element method (MNPBEM) is an open source MATLAB Toolbox simulating of metallic NP, using BEM approach [33, 50, 51]. The main objective of MNPBEM is to solve Maxwell's equations for metallic NPs in the

size range of few to a few hundred nanometers, where the incident wavelength is in the optical and near-infrared regime.

- Finite-difference time-domain method (FDTD)

FDTD a numerical method associated with approximate solutions of differential equations. It is a time-domain solver which means with a single simulation the solution of the whole frequency is developed [52]. Consequently, solving non-linear materials is another advantage of the method. FDTD essentially is similar to finite difference method (FDM) and use the same methodology. For the implementation of FDTD, a computational domain is required. The $\overline{E}$ and $\overline{H}$ fields are calculated at each point of the domain. FDTD is a versatile method with geometry and material. One major weakness of FDTD is the long solution times required. MIT electromagnetic equation propagation (MEEP) is a free and open source FDTD software package developed in C++ to model electromagnetic systems [53]. Didari and Mengüç reported FDTD with near-field radiative transfer contribution in order to account for the thermal effects in the solution of Maxwell's equations [40–42, 54].

- Finite element method (FEM)

The finite element method is a powerful simulation technique to solve boundary-value problems in a variety of engineering problems. It uses subdivision of a whole problem domain into simpler parts (finite elements), and with this technique approximates a complex equation over a large domain by connecting many simple element equations [55]. FEM is similar to FDTD in that it can solve a diverse range of problems, through the long computational time, compares to semi-analytical methods is a major weakness of the method.

- T-Matrix method

The T-matrix method is a semi-analytical CEM method originally formulated by Waterman [56]. The method is also known as null field method. T-matrix approach is one of the most powerful and widely used tools for accurately computing light scattering by nanoparticles. The approach is based on Mie theory [47] and matrix elements match the boundary conditions for solutions of Maxwell's equations. The method is fast and reliable and usable for a wide range of geometries, however, it is unstable for elongated/flattened objects.

- Discrete Dipole Approximation (DDA)

DDA is a semi-analytical method capable of calculating optical properties of inhomogeneous, anisotropic and arbitrary-shaped geometries. DDA method was first introduced by DeVoe [23] for particles much smaller than a wavelength. Later on, Purcell and Pennypacker [24] formulated it without such a limitation. DDA is motivated by the real physical properties of matter. Once an object interacts with an EM field, its atoms start polarizing in the opposite direction of the field. Discrete Dipole Approximation (DDA) is based on defining the object of interest as a collection of discrete dipoles, where atoms of the object are approximated with these dipoles. Dielectric properties of a material are related to the polarization of the individual atoms based on Clausius-Mossotti (or Lorentz-Lorentz) relation, where the same applies to a collection of dipoles [25]. Each dipole in the system is considered to be on a cubic lattice [24]. DDA formulates the interaction between the objects' representative dipoles as a system of linear equations known as the interaction matrix. An object's dipole polarization is calculated by solving the set of linear equation.The system's optical properties and far-field and near-field can be calculated from the dipole polarizations [24, 25]. The limitation of DDA method is for large objects, where many dipoles are needed to reach the desired accuracy, and consequently a large memory is needed. Other limitations are objects with high imaginary parts of refractive indices, where the DDA method overestimates the absorption in the system [25]. The DDA method is also not suitable for objects with large aspect ratios [25]. There are well-known open source packages for DDA such as DDSCAT, written in FORTRAN and developed by Draine and

Flatau [25,26], and ADDA written in C and developed by Yurkin and Hoekstra [27,28]. For the case of objects on a surface, the DDA method developed to calculate the interaction of surface analytically. Note that, DDA formulation for structure on a surface needs special attention. For that reason, the next chapter is devoted to this concept and formulation.

3. Discrete Dipole Approximation with Surface Interaction (DDA-SI)

3.1. DDA-SI Basics

For objects on a semi-infinite surface in the DDA method, we could also model the surface with dipoles. The thickness of the surface should be large enough to be considered as semi-infinite, which would introduce a large number of dipoles in the system. Taubenblatt and Tran [29] instead calculated and added the surface interaction analytically to the formulation of DDA method. Later DDSURF was developed by Schmehl and Nebeker [30, 31]. While these two models are not released as an open source software to the general public, DDA with Surface Interaction (DDA-SI), is an open source MATLAB^{TM} toolbox developed by Loke and Mengüç [32]. In this thesis, we used DDA-SI MATLAB^{TM} toolbox to solve our physical problem. It was the only open source publicly available DDA with surface interaction toolbox. The toolbox has been verified by the authors for plane wave-particle and surface wave-particle interactions against solutions by FEM and FDTD and BEM methods [33, 57]. DDA-SI is verified against FEM in the thesis for particles with larger aspect ratios than the previous verifications, which is a more critical case. Semi-infinite surface and the nature of optimization problem in 3D space made the problem impractical to be solved by FDTD or FEM due to the long computational time required by these methods, and T-matrix method is not stable for modeling elongated objects like surfaces. The ability of analytically calculating the effect of the semi-infinite surface and 3D space optimization made DDA-SI a very practical choice for this study.

3.2. Verification of DDA-SI

As mentioned in Section 3.1, DDA-SI is verified against well-known methods such ad FEM,FDTD and BEM [33,57]. The toolbox also validated against microwave analog experiments [34] for the far-field scattering of non-absorbing and absorbing particles on

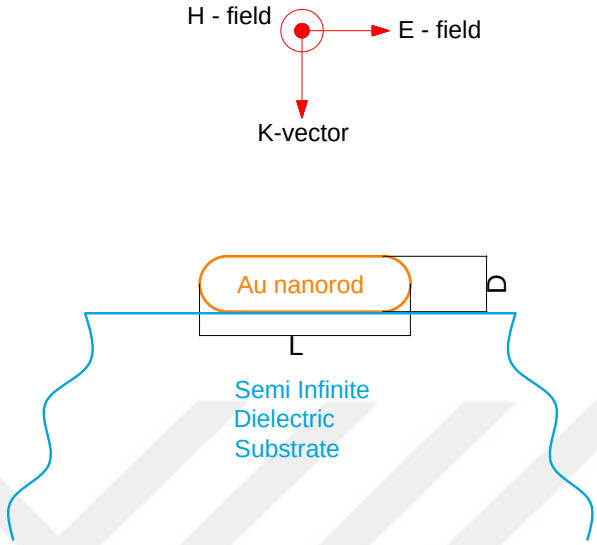

Figure 3.1: Schematic view of a nanorod sitting on a surface under perpendicular TM polarized wave.

a surface. [34]. The verifications were for a 50 nm Au nanosphere on a glass surface; the medium above the substrate were air or water in the reported verifications. Here, we verified DDA-SI against FEM method for an Au nanorod sitting on a surface with air as the medium above the surface. The set-up of the configuration is shown in Figure 3.1. The size parameters of nanorod are $D = 15$ nm and $L = 30$ nm and the system is under a TM-polarized illumination from above the substrate with a perpendicular K-vector to the surface. Refractive index of the substrate is 1.9, while optical properties for gold are obtained from [58], and the incident wave is in the $400 < \lambda < 800$ nanometre range. In the case of an object with a large aspect ratio, the error in calculations by DDA method will rise [25], so a nanorod study case is a more critical case than a sphere reported in the previous studies [33, 57]. The comparison results are shown in Figure 3.2. DDA-SI shows a good match with finite element method for calculation of extinction efficiency (Q_{ext}).

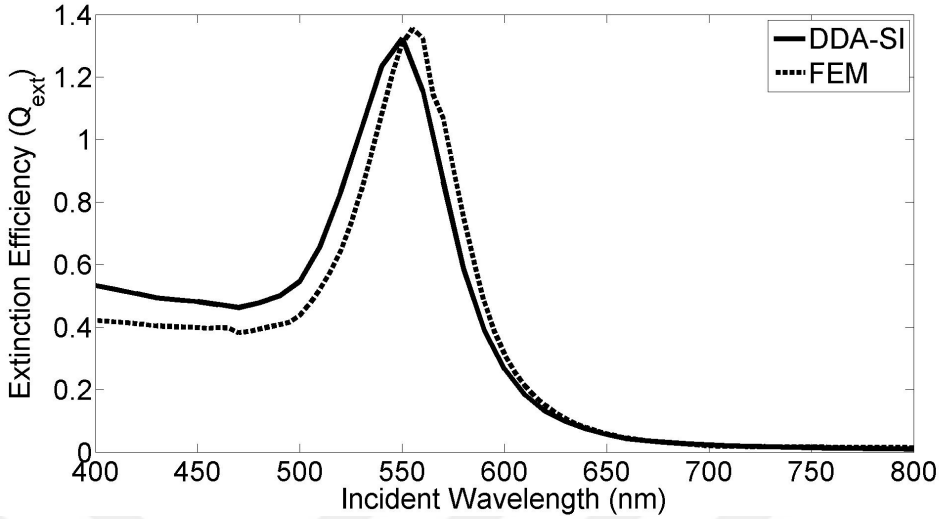

Figure 3.2: Comparing DDA-SI with Finite Element Method (FEM), for extinction efficiency calculation of a nanorod on a dielectric surface.

3.3. Vectorized DDA-SI (DDA-SI-v)

Limitation of computational resources is one of the major challenges of spatial optimization problems. DDA as a semi-analytical method offers a major improvement in solving scattering problems over complete numerical methods. DDA-SI, on the other hand, offers a further improvement integrating the surface interaction via an analytical formulation. However, for tip position investigation in 3D space, computation time demand would be significant as number of dipoles that must be considered to accurately represent the model can be substantial. Therefore, the DDA-SI package functions are modified by adopting linear algebra based formulations that are shorter and more computationally efficient in MATLAB environment in an effort to improve the computational efficiency. Moreover, package functions are also improved for memory usage, by de-allocating the stored intermediate variables after their use. A vectorized and optimized DDA-SI code developed during the course of this study (DDA-SI-v).

A sample analysis is carried out to demonstrate the improvements of modified code. For a single 50 nm AuNP on a BK7 glass surface interacting with a surface wave for a single wavelength of 515 nm (Figure 3.3), the analysis was performed with the

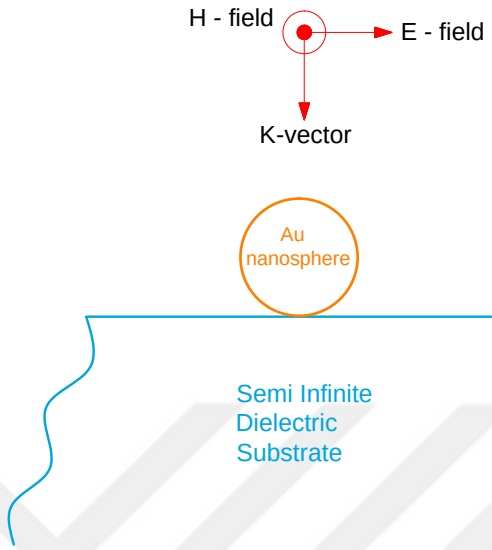

Figure 3.3: Schematic view of a nanosphere sitting on a surface under perpendicular TM polarized wave.

original DDA-SI and modified version(Vectorized DDA-SI). The corresponding computation times and speed up is showed in Figure 3.5. For a single 50 nm dielectric sphere with a refractive index of $\bar{n} = 1.43 + 0i$ on BK7 glass interacting with evanescent wave (Figure 3.4) the light scattering analysis was done for 181 points in space. The enhancements for every dipole number are shown in Figure 3.6. The results show that the modified package is improved 20 times considering the computation time for absorption efficiency calculation and over 30 for far-field light scattering calculation. Here the time ratio is defined as the rate of computation time required by the original code with respect to the modified code. The analysis was carried out using a system with 2 GHz CPU.

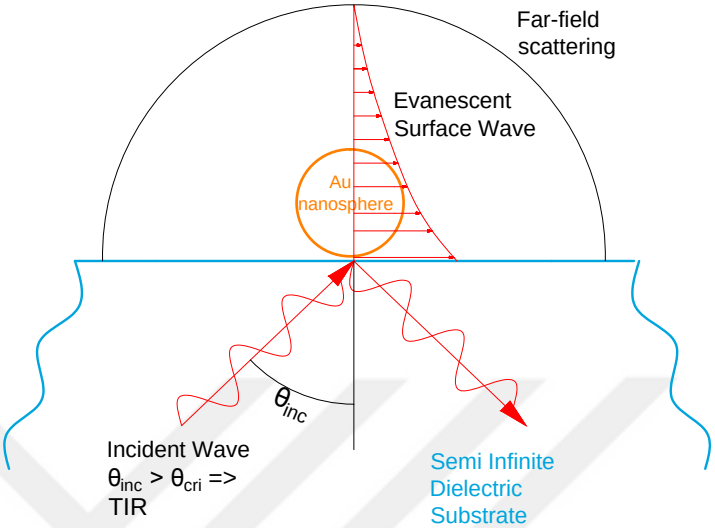

Figure 3.4: Schematic view of a nanosphere sitting on a surface under surface evanescent wave.

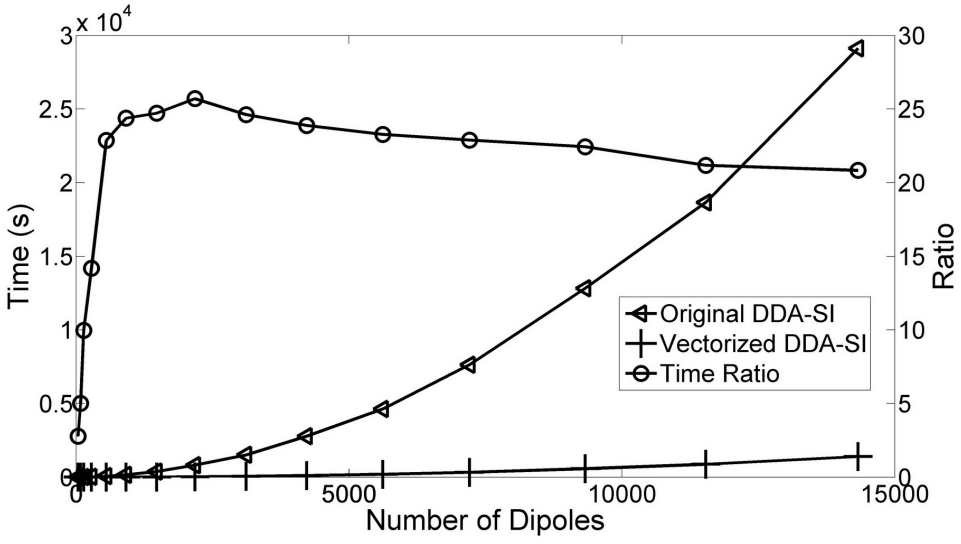

Figure 3.5: Original and modified (vectorized) DDA-SI comparison for different number of dipoles of a sphere on a surface interacting with an evanescent wave at its resonance point. The right y-axis is showing the computational time ratio between the original and modified packages.

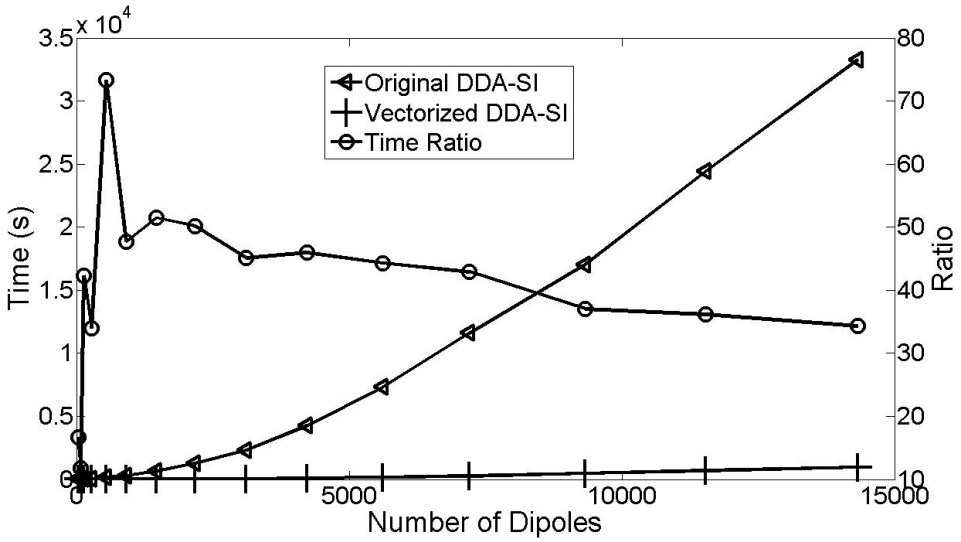

Figure 3.6: Original and Modified (Vectorized) DDA-SI comparison for light scattering calculation of a dielectric sphere on a dielectric substrate. The far-field scattering calculated for 181 points in the space. The right y-axis is showing the computational time ratio between the original and modified packages.

4. Enhancing Local Absorption Patterns Within Gold Nano-structures on a Dielectric Surface Under an AFM probe and With Evanescent-Wave Illumination

4.1. Problem Statement

A 50 nm AuNP placed on a BK7 glass substrate under an AFM tip is considered as shown in Figure 4.1. A monochromatic TM wave incident from underneath the substrate with a 45° incidence angle. As the incidence angle is greater than the critical angle for the range of incident wavelengths between 300 nm to 800 nm, consequently a decaying evanescent wave propagating on the surface and interacting with NP [59]. The pencil-shaped AFM probe tip is made of Si and has a cone angle of 16.7° with a tip radius of 10 nm and a shaft diameter of 50 nm. The spherical NP's position over the substrate is taken as the origin of the Cartesian coordinate system and the position of the tip (x_{tip}, y_{tip}, z_{tip}) is considered in 3D space. In the case of evanescent illumination, the wave field decays moving away from the surface. Therefore, increasing the height of truncated tip over a particular height does not change the absorptivity of NP more than 5% [37].

The system is initially analyzed to ensure adequate number of dipoles is used to represent NP and probe. While using too many dipoles will increase required computational time, using too few will lead to an inaccurate representation. Then, the system response with changing shaft length is evaluated to find a reasonable size for truncating the shaft. The AuNP's absorption behavior is analyzed for different tip positions. While optical properties for gold are obtained from [58], Sellmeier equation, which is an empirical relation between refractive index and wavelength for a particular transparent medium, is used for obtaining BK7 glass optical properties. Spectral refractive index of Silicon is adopted from [60].

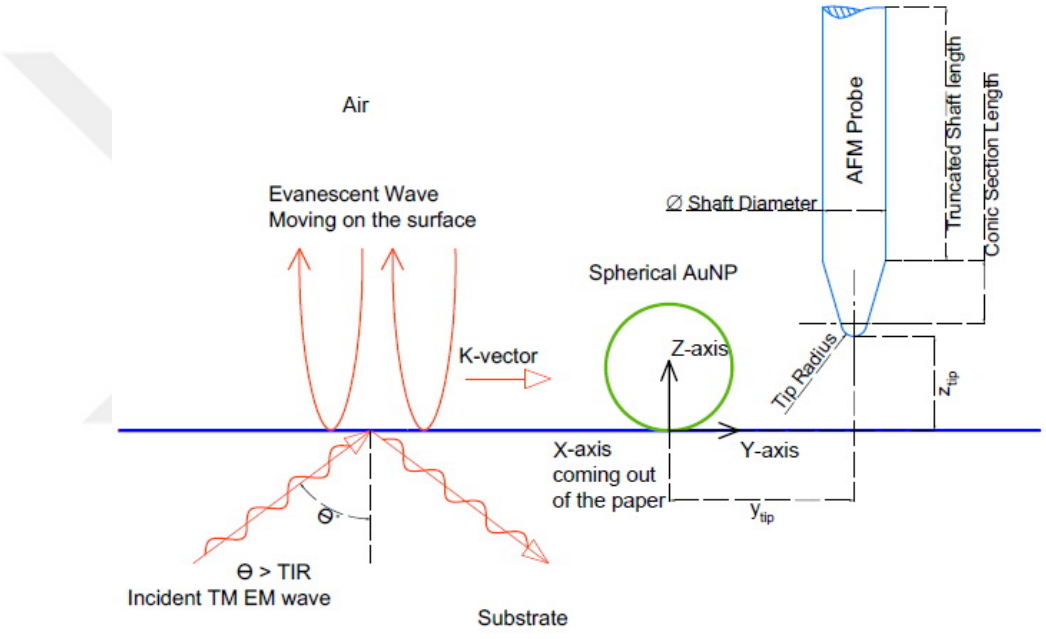

Figure 4.1: A Cross-sectional schematic of the configuration.TM wave is incident at an angle larger than that required for TIR from underneath the BK7 glass substrate. Since the EM wave is TM polarization the decaying evanescent wave has both z and y components.

4.2. Number of Dipoles and AFM Tip's Shaft Length

Dielectric properties of a material are related to the polarization of the individual atoms based on Clausius-Mossotti (or Lorentz-Lorentz) relation. Discrete Dipole Approximation (DDA) is based on defining the object of interest as a collection of discrete dipoles, where atoms of the object are approximated by these dipoles. The dipoles are placed according to a cubic lattice configuration based on a lattice parameter, d, in both DDA and DDA-SI. A sufficient number of dipoles must be used to represent the behavior of the atoms correctly and there are two main criteria for determining the sufficient number of dipoles in DDA [25]. Based on the first criterion,

$$d \leq 1/(|k|\eta) \tag{4.2.1}$$

where k is the imaginary part of the refractive index, d is lattice parameter, and η is the wavenumber. The second criterion is considered when $k > 1$, where DDA can overestimate absorption cross section even if the first criterion is satisfied [25]. For spherical nanoparticles the number of dipoles satisfying the first criterion can be expressed as:

$$N \geq \frac{4\pi^4}{3}\left(\frac{|\ k\ |\ D}{\lambda}\right)^3 \tag{4.2.2}$$

where D is the diameter of the spherical nanoparticle, λ is the wavelength, and N is the minimum required number of dipoles to satisfy the first criterion. The imaginary part of refractive index of Au increases linearly after 500 nm that, necessitate the use of larger number of dipoles for higher wavelengths. For a 50 nm spherical AuNP, $N > 10$ satisfies the first criterion for the visible light range. The required number of dipoles for different sized spherical AuNPs is presented in 4.2.

The second criterion is considered when $k > 1$, where DDA can overestimate absorption cross section even if the first criterion is satisfied [25]. Although there is no direct expression of it, based on the second criterion sufficiently large number of dipoles

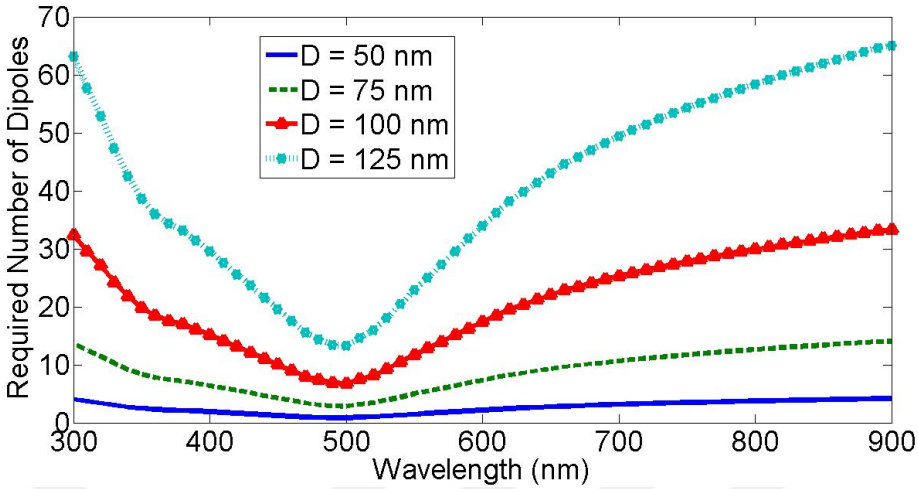

Figure 4.2: Number of dipoles satisfying the first criterion for spherical AuNP, for different sphere diameters, as a function of wavelength.

must be used so that further increasing the number of dipoles does not have an effect on predictions. The second criterion is the main criterion that must be considered as the first criterion can be satisfied by using small number dipoles as shown in Figure 4.2. Therefore, absorption efficiency, Q_{abs}, of the AuNP on a substrate is predicted using different number of dipoles evaluate and identify the number of dipoles satisfying the second criterion. The absorption efficiency, Q_{abs}, is defined as the ratio of the effective cross-section to the geometrical cross-section and it is used as a metric for identifying the number of dipoles satisfying the second criterion. The absorption efficiency is predicted for the AuNP using different number of dipoles. As sufficiently large numbers of dipoles are used, the predicted absorption efficiency converges and does not change with the further increasing number of dipoles. This approach is analogous to grid refinement analysis adopted in computational fluid dynamics.

For a single AuNP placed on a BK7 glass, the absorption efficiency varies as number of dipoles are changed from N=81 to N=2176, as shown in Figure 4.3. However, the general trend and quantities of absorption efficiency in the range, from 300 nm to 800 nm, does not change significantly with changing number of dipoles. The absorption efficiency and relative error are estimated for 4 different wavelengths as a function of number of dipoles and results are presented in Figure 4.4, where the relative error is

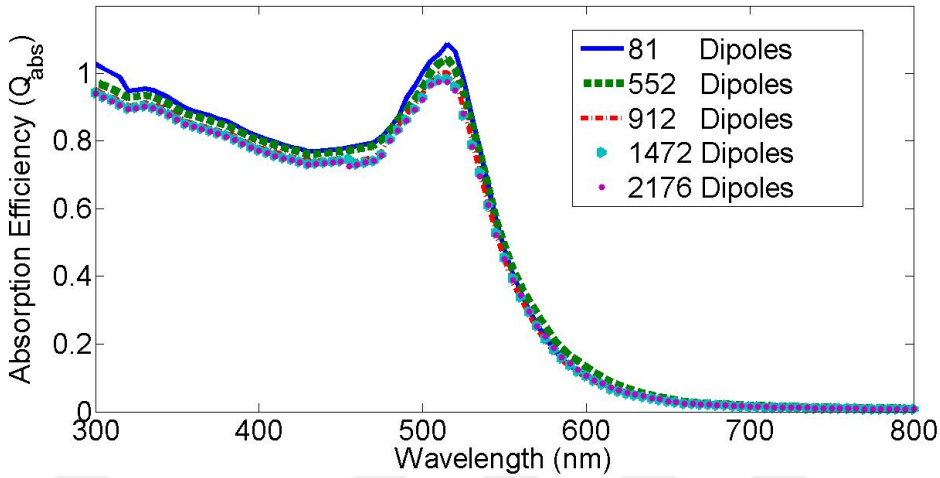

Figure 4.3: Change of absorption efficiency for a single 50 nm AuNP as a function of wavelength for different number of dipoles.

estimated based on absorption efficiency predicted by using 11536 dipoles. For the rest of the analysis, the incident wavelength of 515 nm, which is the resonance wavelength of AuNp, is considered. Using 552 dipoles leads to a relative error less than 12% for the wavelength of interest for a single NP as observed in Figure 4.4.

A similar concern exists for identifying the AFM tip's shaft length. The shaft length of AFM tip can be considered as infinitely large in comparison to NP size. However, for numerical modeling of the system, a size that is both computationally feasible and resulting in acceptable accuracy must be identified and used. Therefore, the proper size must be identified so that further increasing the shaft length does not have an effect on the predictions. Considering that the lattice spacing parameter, d, is constant for the whole system

$$d = \left(\frac{V_{NP}}{N_{NP}}\right)^{1/3} = \left(\frac{V_{AFM}}{N_{AFM}}\right)^{1/3} \tag{4.2.3}$$

where V is the volume. The generated evanescent wave as the result of TIR is decaying exponentially on the surface [59]. For a tapping-mode Si tip, Huda et al. considered 370 nm for the truncated shaft [36]. For a 50 nm AuNP and $N_{NP} = 552$, the lattice spacing is, $d = 4.9127$ nm. For $\lambda = 500$, and the tip is initially placed 2 nm above the

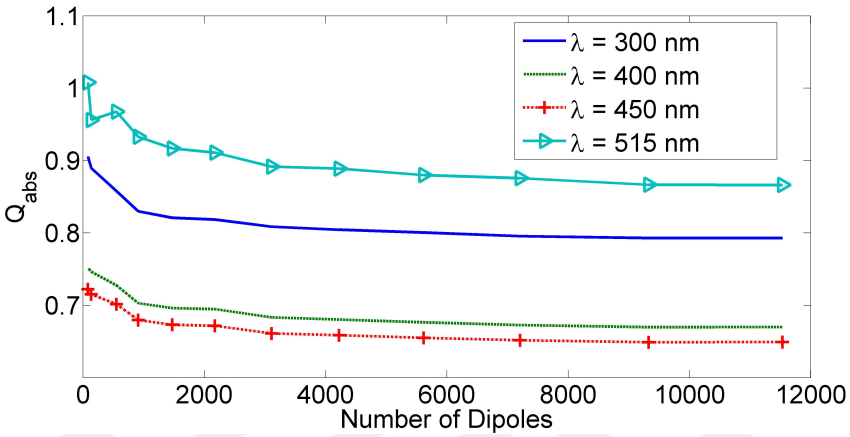

(a)

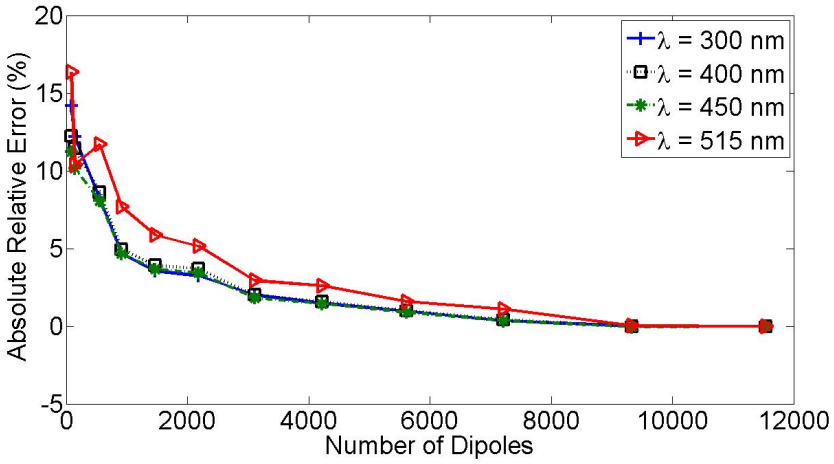

(b)

Figure 4.4: (a) Change in estimated absorption efficiency (Q_{abs}) with number of dipoles (N) for four different incident wavelengths. (b) Change in absolute relative error with number of dipoles for four different incident wavelengths.

NP ($z_{tip} = 52nm$), the length of truncated shaft is changed from 50 nm to 1350 nm and the results are presented in Figure 4.5(a). The predicted absorption efficiency for AuNP oscillates with changing shaft length as a result of the superposition of EM-waves interacting with particle and probe, directly and through the substrate. According to the results presented in Figure 4.5(b), using a truncated shaft length of, $L_{shaft} = 390$ nm will result in less than 5% error, which is adequate for modeling the system. The relative error is defined relative to the absorption efficiency predicted for maximum shaft length considered. As the tip moves upward in the z-direction, it is expected that after a certain distance from the substrate, the near-field the effect of tip's existence on AuNP becomes negligible and absorption efficiency of AuNP converge to the value for single AuNP. This effect can be seen in Figure 4.6 for three different incident wavelengths.

A final analysis is carried out to check if sufficient number of dipoles is used for representing the complete system. The change in the absorption efficiency for the NP is estimated with two different numbers of dipoles for sphere and tip with the identified truncated length of 390 nm in Figure 4.7. While the tip touches the substrate ($z_{tip} = 0$ nm), it changes position around the AuNP. Incident wavelength is 515 nm, which is the resonance wavelength for AuNP. The contour plots, showing the overall absorption efficiency with different tip positions has the same pattern; however, there is a slight shift in values. According to these results, it can be concluded that using $N_{NP} = 552$ and $N_{AFM} = 6787$ can estimate absorption efficiency of the nanoparticle in the presence of tip with an acceptable error while preserving the pattern of absorption behavior this research is exploring.

4.3. Results and Discussions

4.3.1. Au Nanoparticle Interaction with Si Tip

After determining appropriate dipole numbers ($NNP = 552$ and $N_{AFM} = 6787$) and shaft length of truncated tip's ($L_{shaft} = 390$ nm) AuNP's absorption behavior as a function of tip location in 3D space is investigated in more detail. The previous

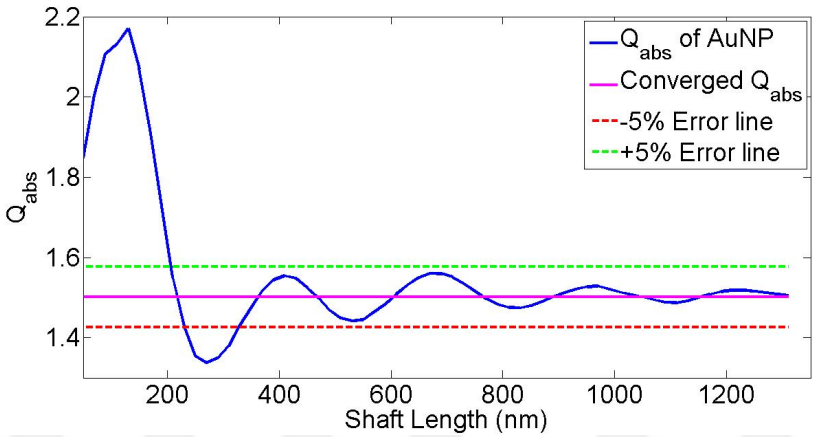

(a)

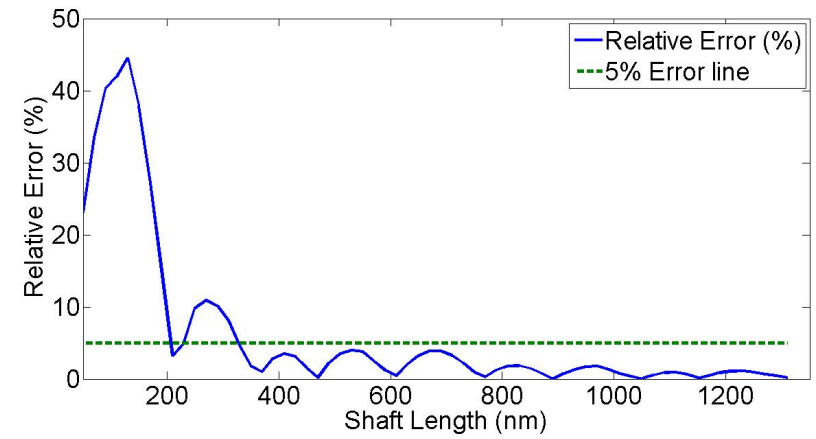

(b)

Figure 4.5: (a) Change of absorption efficiency of AuNP with the changing silicon tip shaft length. (b) Relative error with changing shaft length.

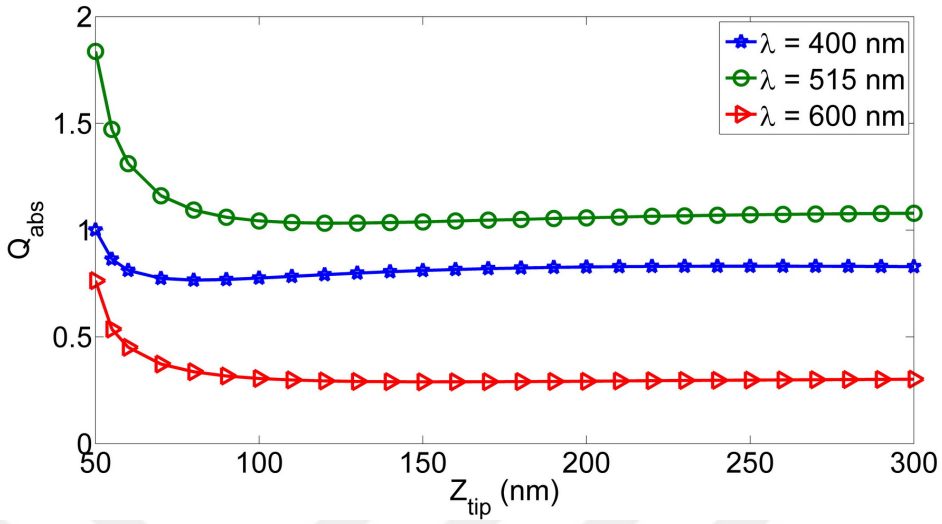

Figure 4.6: Change of absorption efficiency for the AuNP as the truncated shaft vertically moves upward for different three wavelengths of the incident beam.

study by Huda et al. was carried out by Finite Element Method (FEM) and showed that a tapping-mode Si tip does not change the LSPR of a 50 nm AuNP on BK7 substrate with incident surface evanescent wave [37]. The absorption behavior using Si tip is plotted in Figure 4.8 for three different tip positions. The absorbing behavior of silicon between 300 nm to 400 nm is not negligible, which leads to metal to metal like near-field interaction that usually damps the oscillatory behavior of NP's plasmonic response. Achieving these phenomena is desirable for applications such as imaging and sensing, where heat absorption should be reduced. It can be observed in Figure 4.3 that the single AuNP experience resonance mode at one particular incident wavelength. However, it can be observed in Figure 4.8 that NP is reaching another resonance mode at an incident wavelength of 380 nm. This resonance is due to the near-field interaction with the Si tip. The imaginary part of refractive index of Si is negligible after incident wavelength of 450 nm and Si behaves like a dielectric, where Si tip enhances the absorption peak of AuNP. Consequently, the resonance wavelength of AuNP does not change and the analysis can be carried out considering the same wavelength to maximize the heating.

In order to identify the optimal tip location to maximize localized heating of

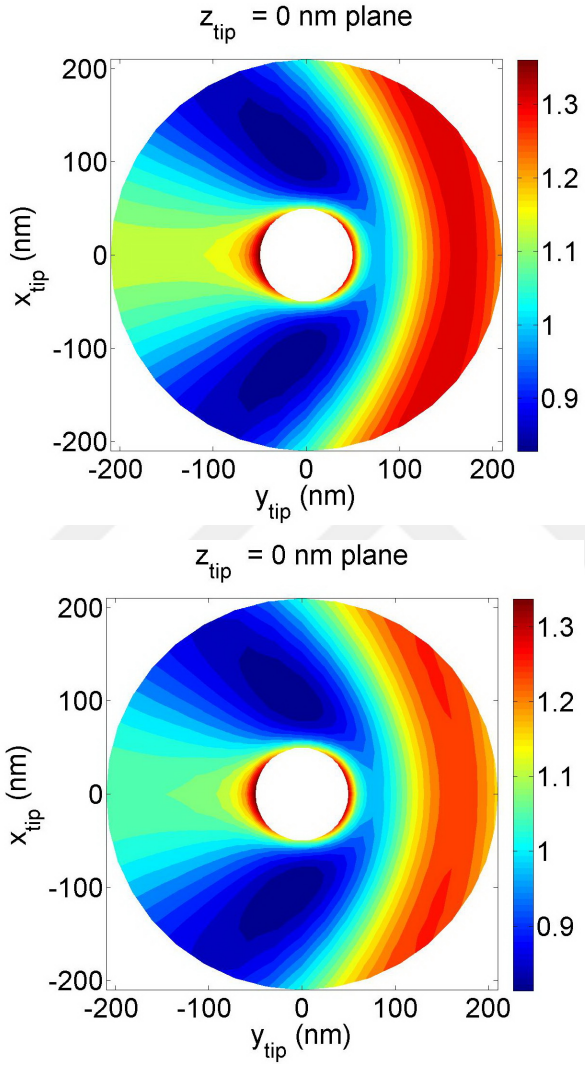

Figure 4.7: Absorption efficiency patterns at different tip positions in a fixed height around the AuNP for two different particles and probe number of dipoles. a) Number of dipoles for sphere and tip is 81 and 882, respectively. b) Number of dipoles for sphere and tip are 552 and 6787, respectively.

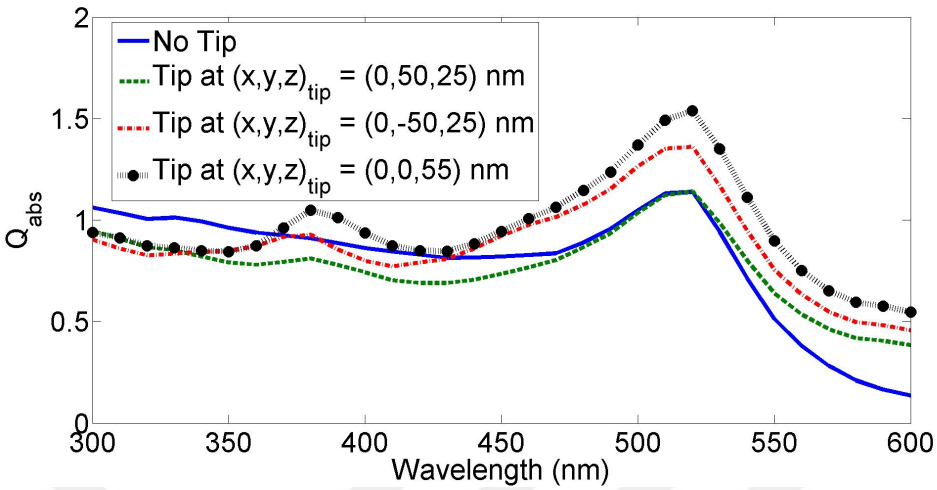

Figure 4.8: Change in Q_{abs} of AuNP versus incident wavelength in the presence of tip at three different locations. Si tip does not affect the resonant point of 50 nm AuNP at 515 nm and simply enhance the magnitude.

AuNP, Q_{abs} is estimated with changing tip location around the AuNP at a constant height above the surface (z_{tip}= constant) and the incident wavelength is fixed at 515 nm which is around resonance point. The Q_{abs} for the case tip is touching the substrate (z_{tip}=0) is presented in Figure 4.9(a). Next, similar results are presented for heights for z_{tip} = 25 nm and 50 nm in Figure 4.9(b) and Figure 4.9(c), respectively. In each plot, a 25 nm clearance distance between the tip and AuNP is considered. It can be observed that the general trend of the absorption for AuNP is similar for different tip heights. However, as the tip is closer to the surface, the coupling is stronger and the values increase. The maximum value of absorption happens when the tip is in the vicinity of AuNP. Locating the tip in front of the AuNP relative to the wave vector of the surface wave, where the wave first interacts with the tip and then the AuNP. Heat absorption by the particle can be increased by approximately 40% compared to the single AuNP at resonance wavelength showed in Figure 4.3, However, controlling the tip with such a precision could be a challenging task at the nano-scales considered. In the case when controlling the tip location precisely in the vicinity of AuNP is challenging, an alternative approach appears to be locating the tip at a distance between 160 nm to 200 nm in the back of the NP, relative to the surface wave vector direction, where the wave first interacts with the NP and then the tip. This approach can increase the heat

absorption by NP by around 25%. It can also be observed that there are regions where the tip has a negative effect on the absorption.

The change in the overall absorption efficiency of NP for the case where the tip is moving in the $x_{tip} = 0$ plane is presented in Figure 4.10. The clearance between NP and tip at the sides and top is considered as 25 nm. It can be observed that lowering the probe height has a positive effect on heating of NP. These trends also confirm the conclusions in regards to ideal tip locations relative to AuNP and wave vector of incident illumination. The tip has maximum effect when it is located by the side of the NP in the direction of the incident wave. If the tip can precisely be controlled and it is possible to bring in closer proximity of the NP, higher values of absorption efficiency can be achieved. To demonstrate this, the analyses are extended for a clearance distance of 2 nm from the top and the results are presented in Figure 4.11.

While the results presented up to here considers overall or spatially integrated absorption efficiencies, localized normalized field distribution over the NP based on the K-vector and tip position is also considered. The dipole's normalized field intensity is directly related to absorbing effect and consequently heat absorbed by that dipole. Extrapolating normalized field intensity over a spherical AuNP, the heat absorption by the NP is estimated that can be used for solving the energy equation for the NP. The surface of the sphere is responsible for most of the absorption due to free electrons on the surface of metals, as can be observed in Figure 4.12 that presents local intensity contours.

In our problem definition, K-vector is defined in positive $y-$axis direction (Figure 4.1) leading to symmetry in the dipoles' electrical field with no tip condition. Whereas for the case, $x_{tip} = 0$, the symmetrical behavior of the system is still preserved. The dipole normalized intensities extrapolate over the sphere surface and the circular cut on the $x = 0$ plane, where the sphere is modeled using 552 dipoles in this study. In the case of single NP without tip, it can be observed in Figure 4.12(a) that the intensity is higher on the surface of the sphere and especially in the parts that first interacts

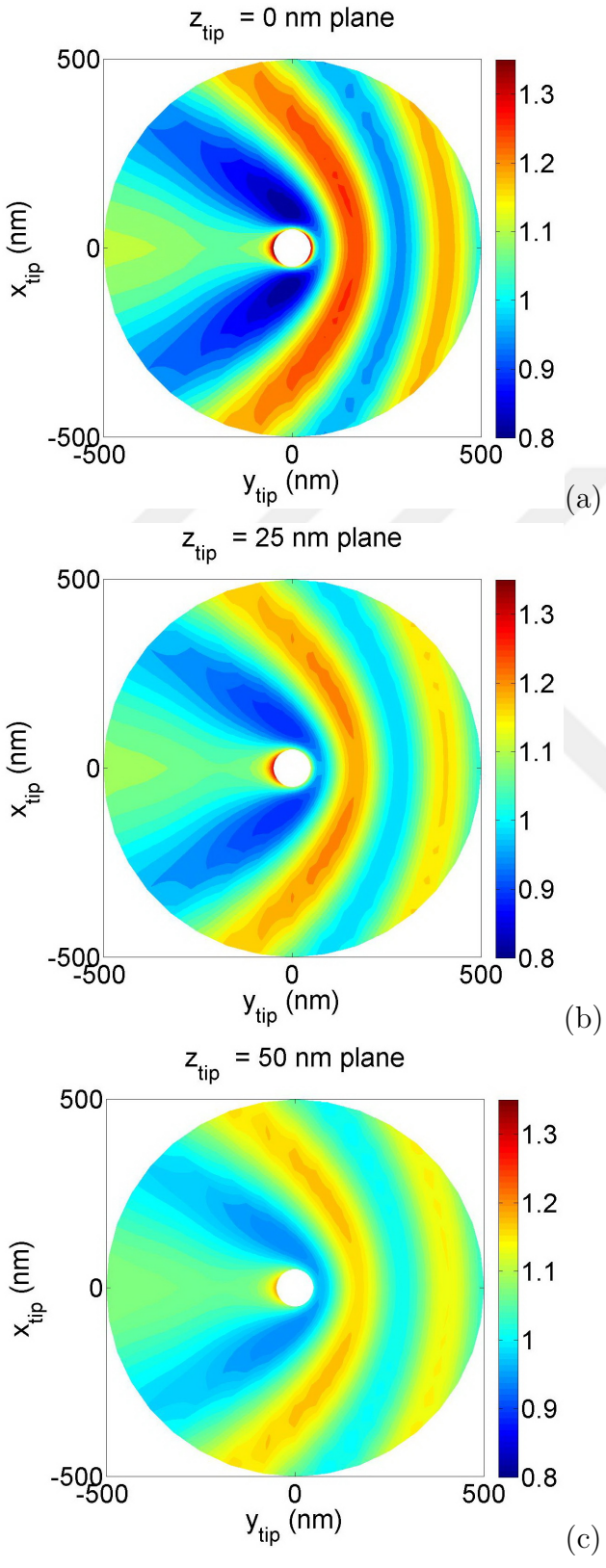

Figure 4.9: Change of absorption efficiency of AuNP as a function of tip position in different x_{tip} and y_{tip} coordinates for three fixed z_{tip} values.

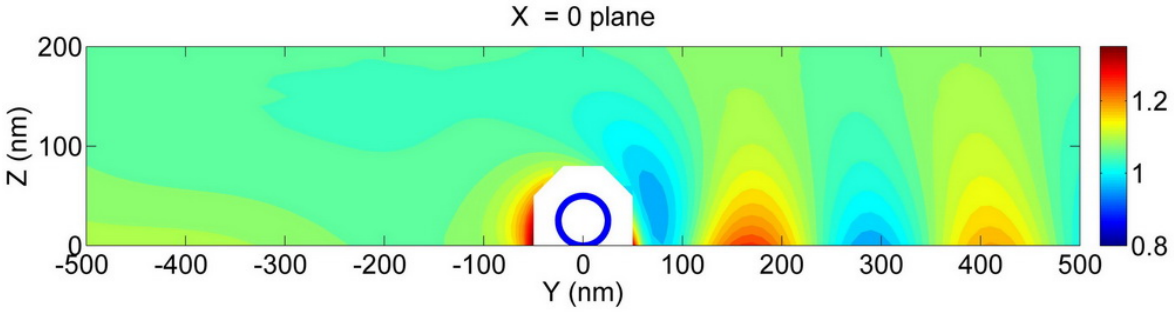

Figure 4.10: Absorption efficiency of AuNP for different tip positions on $x_{tip} = 0$ plane. Blue circle represents the spherical NP.

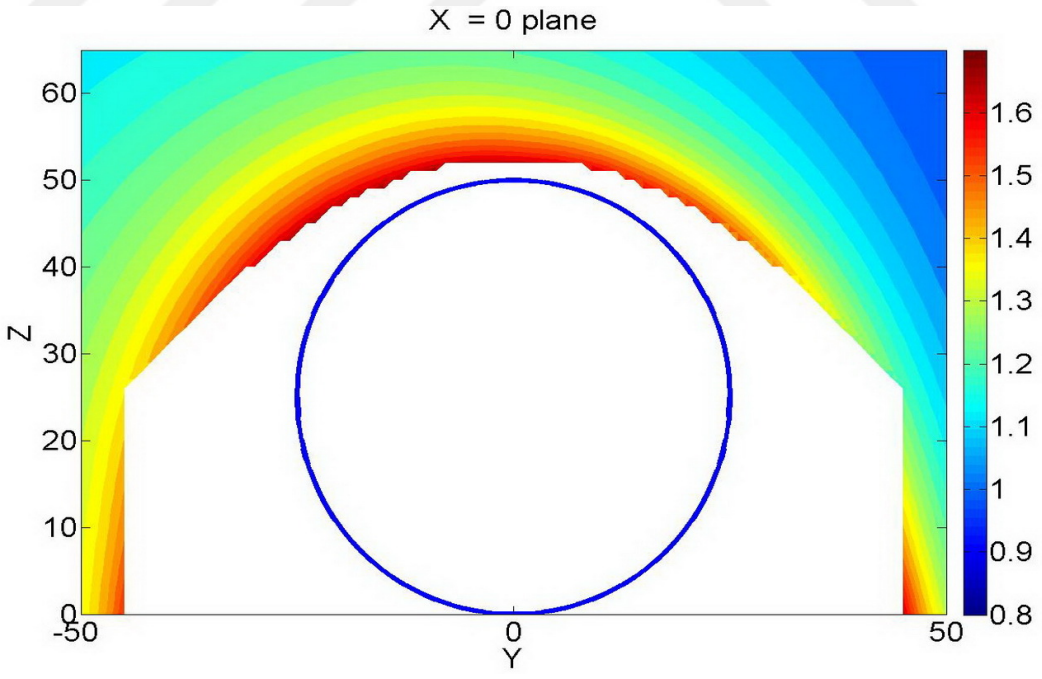

Figure 4.11: Absorption efficiency of AuNP for different tip positions on $x_{tip} = 0$ plane. Blue circle represents the spherical NP.

with the surface wave. The core area of the sphere has low intensity leading to low absorption and the dielectric surface has no visible field intensity localization effect. When the tip is placed above the NP, $(x_{tip}, y_{tip}, z_{tip}) = (0, 0, 52)$ nm , the absorption locally intensifies at the upper part of the NP as can be seen in Figure 4.12(b) with tip presence vividly bringing a sharp gradient in overall heat generation in the NP. When the tip is at the position, $(x_{tip}, y_{tip}, z_{tip}) = (0, -45, 0)$ nm, the wave first interacts with the tip and then the NP as shown in Figure 4.12(c) and the local electrical field intensifies at the surface of the sphere, in the region approaching from negative $y-$axis direction. Whereas if the tip is at the position, $(x_{tip}, y_{tip}, z_{tip}) = (0, 45, 0)$ nm, the incident wave first interacts with NP and then with the tip. The maximum intensity shifts towards the positive y-axis direction as can be observed in Figure 4.12(d). For this tip position, the absorption efficiency enhancement is less than the other cases, based on results presented in Figure 4.10. The direction of the incident wave and the position of the tip both bring a localized heat generation effect. However, from the plots, it is observed that the position of the tip is more important than the K-vector direction. The largest value of normalized field intensity is observed in Figure 4.12(c), due to the combined localization effect of the tip and surface wave direction leading to the highest gradient in absorption over the NP. Based on Figure 4.10, this tip position also leads to the largest overall absorption efficiency value.

4.3.2. Core-Shell Au-SiO_2 Nanoparticle Interaction with Si Tip

As stated earlier, it can be presumed that core-shell NP with an optically dense dielectric core could offer an improvement for overall absorption although the core does not effectively participate in absorption. The dielectric core will be polarized due to the incident beam that will interact with the absorbing shell, leading to a change in plasmon resonance and improvement in absorption. The concept was proven by the studies focusing on photothermal cancer therapy using core-shell NPs [61], which consider their enhanced heat absorption for heating of nano-scale objects using laser irradiation by providing a means of enhancing absorption or heating of single NPs in liquid for mainly cancer therapy applications [61–63].

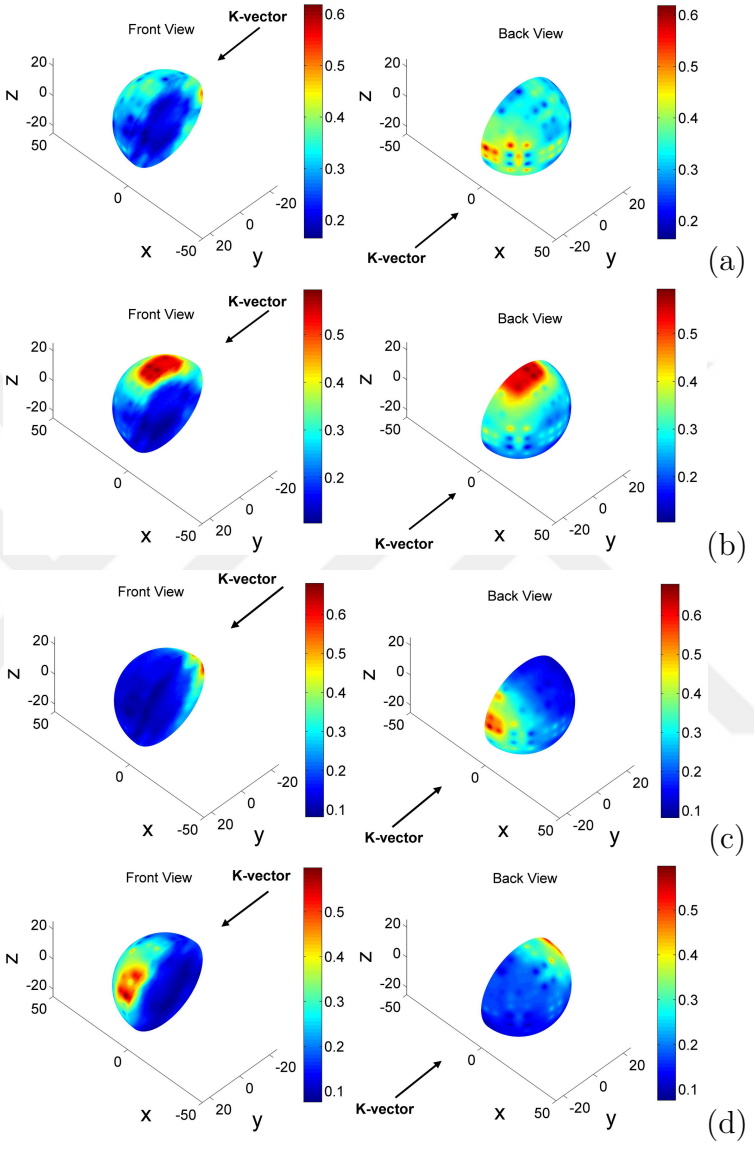

Figure 4.12: AuNP dipole normalized field intensity extrapolated on the surface of the sphere and on a cut on $x = 0$ plane. There is symmetry on the $x-$axis so only a hemisphere is shown. Each case is shown in two opposite views with respect to K-vector. (a) Single AuNP without tip. (b) Tip is positioned at the top of NP at position $(x_{tip}, y_{tip}, z_{tip}) = (0, 0, 52)$ nm. (c) Tip is positioned at $(x_{tip}, y_{tip}, z_{tip}) = (0, -45, 0)$ nm. (d) Tip is positioned at $(x_{tip}, y_{tip}, z_{tip}) = (0, 45, 0)$ nm.

Therefore, the effect of SiO_2 core in the NP absorption behavior is also investigated in this study, where optical properties of SiO_2 are obtained from [60]. Core-shell NP considered has an outer diameter of 50 nm with different SiO_2 core diameter sizes. Considering the discrete nature of dipoles on DDA analysis, the effect of number of dipoles used in the simulation on different core sizes for an incident wavelength of 500 nm is presented in 4.13. The results show that for a core diameter of 35 nm, using over 2000 dipoles for the simulations will result in a relative error that is less than 5%. As in the earlier case, the relative error is estimated based on estimations using 11536 dipoles. Similarly, for 20 nm, 25 nm and 30 nm the relative error is less than 5% when more than 552 dipoles are used for simulation. Therefore, 2176 dipoles are used for NP, which leads to a lattice spacing of d = 3.11 nm for capturing the effect of the dielectric core in the simulations. For single SiO_2 core-Au shell NPs (with no tip) sitting on BK7 surface interacting with an evanescent wave, the resonance wavelength red-shifts when compared to that for the single AuNP without a core (Figure 4.14). The maximum absorption at the resonance wavelength is observed between core diameters of 30 nm to 40 nm and for the case of a single core-shell particle with 35 nm diameter SiO_2 core, absorption improves approximately 30% with respect to the case of solid AuNP as shown in Figure 4.14. The effect of the tip in conjunction with the core-shell NP is investigated next. A core-shell NP with 30 nm diameter SiO_2 core, coated with 10 nm Au shell is considered together with a truncated Si tip with a length of 410 nm. Absorption efficiency is evaluated for the wavelength band of 400 nm to 600 nm for 3 different tip positions. The results show over 70% improvement in the absorption of NP in the case of dielectric core and tip compared to single, 50 nm solid AuNP sphere at their respective resonance wavelengths as shown in 4.15.

The intensity field plots presented in Figure 4.16 show that presence of the dielectric core makes the intensity in the Au shell more homogeneous. This can be clearly seen, comparing Figure 4.12(a) with 4.16(a). Moreover, bringing the tip in the vicinity of core-shell NP has a less localized heating effect, which can be comprehended by comparing Figure 4.12(b) with Figure 4.16(b). Therefore, considering the heat transfer analysis in the NP, having a core enhances the total heat absorption by the particle, and it would lead to uniform heating of NP's Au shell, preventing high-temperature

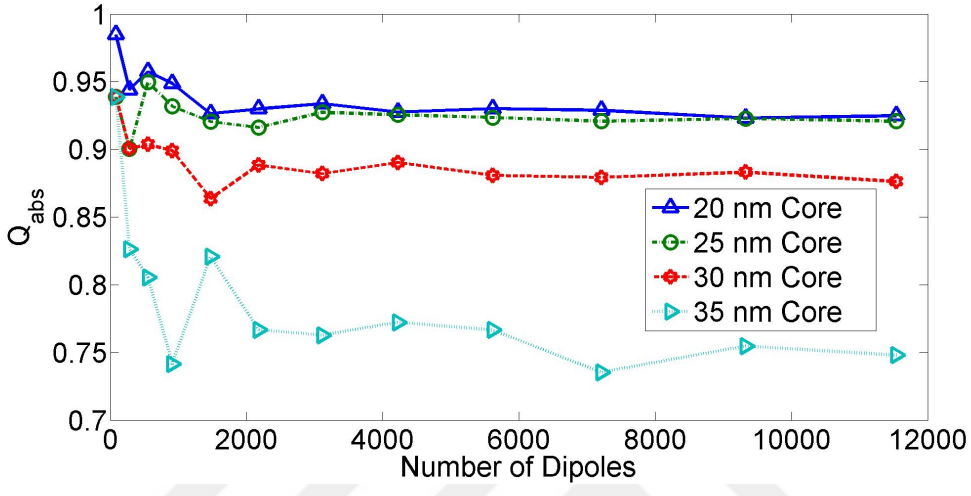

(a)

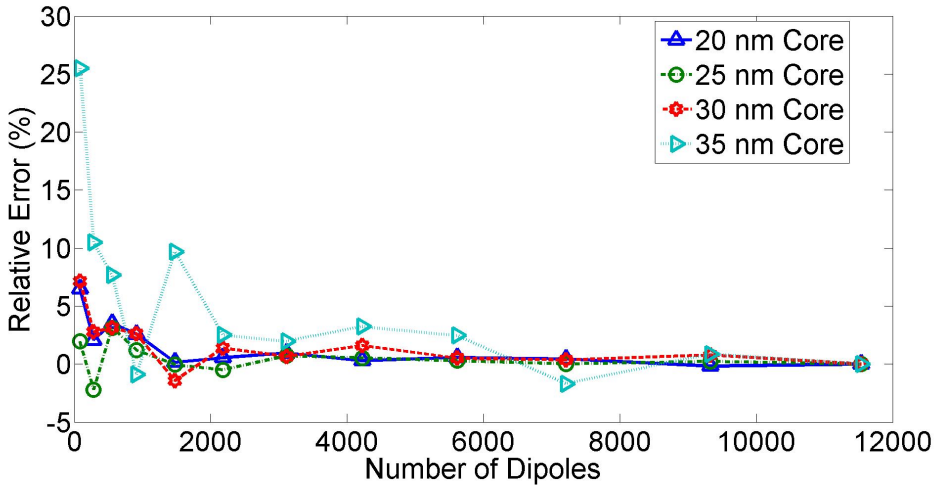

(b)

Figure 4.13: (a) Absorption efficiency of a 50 nm core-shell NP with SiO_2 core and Au shell for three different core diameters estimated using different number of dipoles for fixed incident wavelength of 500 nm. (b) The relative error of predicted absorption efficiency by using different number of dipoles calculated based on estimations using 11536 dipoles.

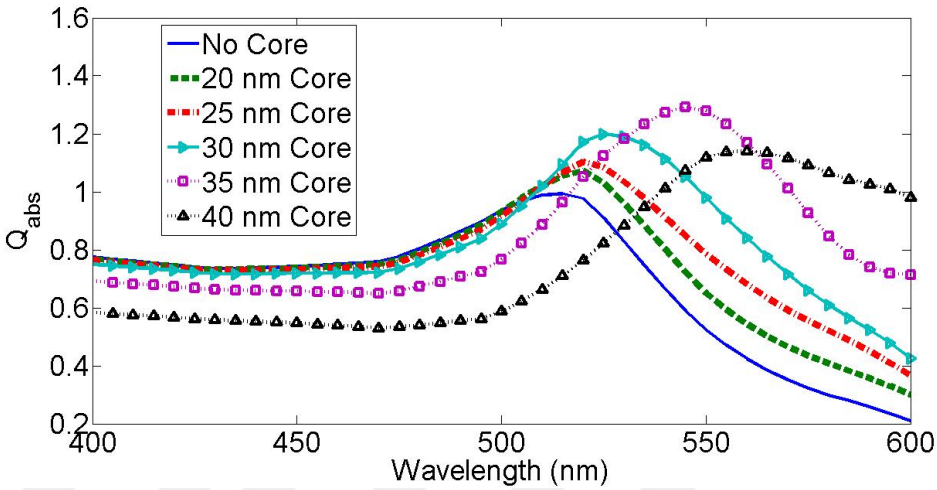

Figure 4.14: Comparison of single 50 nm NP with different SiO_2 core diameters as a function of wavelength.

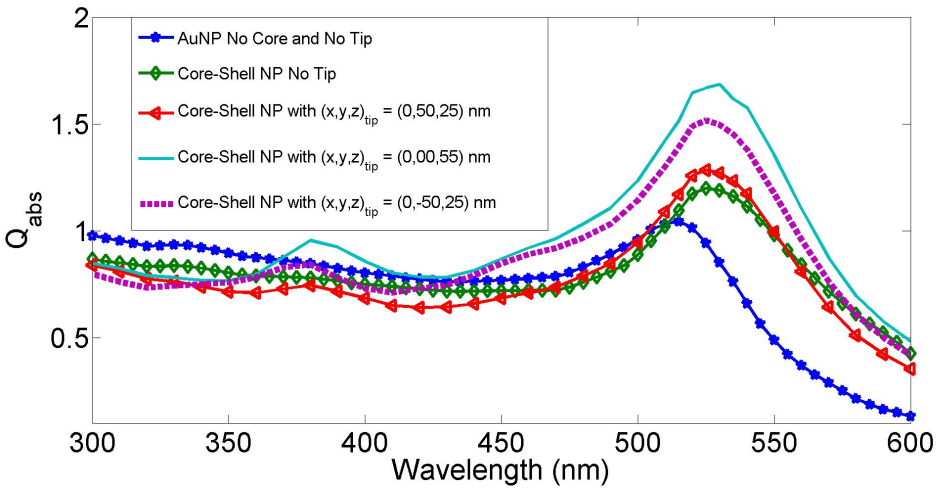

Figure 4.15: Q_{abs} as a function of wavelength for different tip positions in space for 30 nm SiO_2 core in a 50 nm diameter NP with shell made of Au.

gradients across the shell.

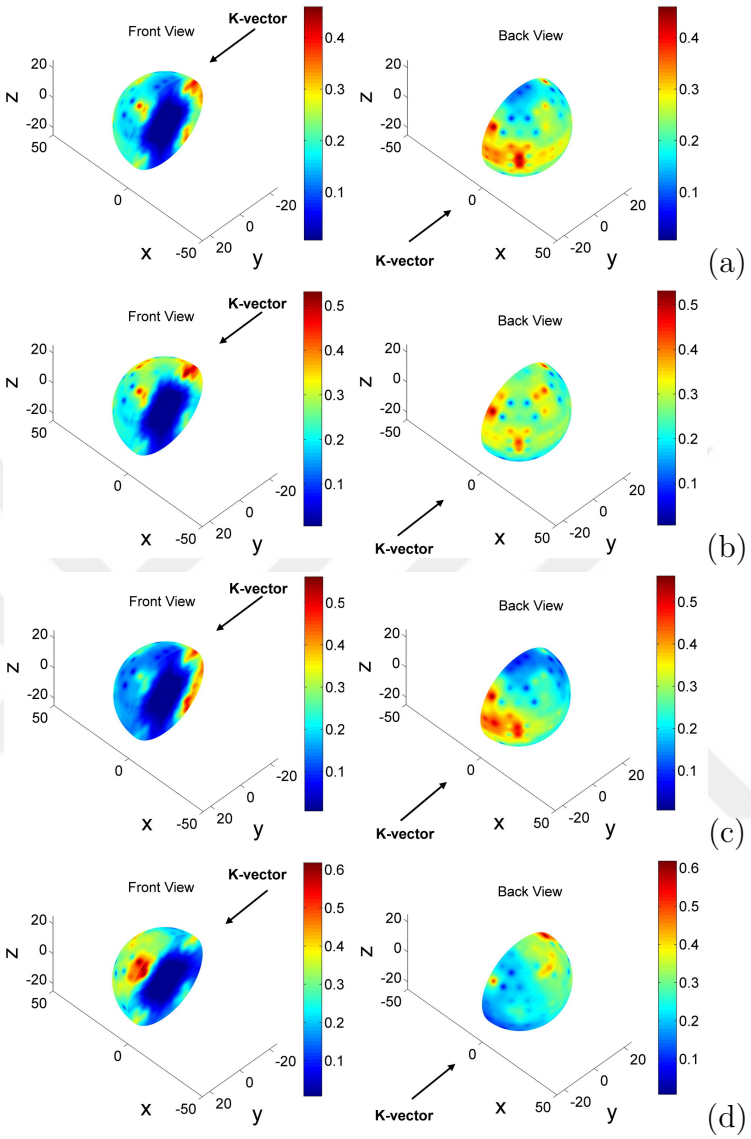

Figure 4.16: Core-shell Au-SiO_2 NP with core diameter of 35 nm normalized field intensity extrapolated on the surface of the sphere and a cut on plane $x = 0$ plane. There is symmetry on the $x-$axis so only a hemisphere is shown. Each case is shown in two opposite views with respect to K-vector. (a) Single core-shell without tip. (b) Tip is positioned at the top of core-shell NP at position $(x_{tip}, y_{tip}, z_{tip}) = (0, 0, 52)$ nm. (c) Tip is positioned at $(x_{tip}, y_{tip}, z_{tip}) = (0, -45, 0)$ nm which the incident evanescent wave first interacts with the tip and then the core-shell NP (d) Tip is positioned at $(x_{tip}, y_{tip}, z_{tip}) = (0, 45, 0)$ nm which the incident evanescent wave first interacts with the core-shell NP and then the tip.

5. Conclusions and Future Work

5.1. Conclusions

Local heating of nanoparticles for precise nano-manufacturing processes is numerically explored by analyzing the absorption patterns within nanostructures on glass surfaces. Improvements have been introduced to previously released toolbox Discrete Dipole Approximation with Surface Interactions (DDA-SI) [32]. However, the new code, which is called DDA-SI-v, is optimized that the computations can be carried out more efficiently in vectorized format. In the present thesis, DDA-SI-v is used for evaluating of the effect of an AFM tip on nanoparticle on a surface. The current DDA-SI-v is a general package that can be used to calculate optical properties by any type of particle on a surface.

It is assumed that a tip of atomic force microscopy facilitated the process as a means of controlling localized heating. The effect of dielectric (Si) AFM tip on the absorption of a gold nanoparticle on BK7 glass substrate with air as medium above the substrate is analyzed for surface decaying evanescent illumination. Si AFM tip can effectively increase heat absorption in the nanoparticle, especially for the case where the tip is located in close proximity of the substrate and in the back of nanoparticle relative to the direction of the wave vector. The optimum position of an AFM probe around a nanoparticle is identified through simulations, leading to highest absorption by nanoparticle. While the surface of the gold nanoparticle is responsible for most of the absorption, it was shown that placing a dielectric core in the gold nanoparticle can increase the absorption. The optimum core diameter is evaluated and the interaction of core-shell gold nanoparticle with silicon tip is analyzed. The presence of dielectric core can improve the uniform heating of nano-structure and prevent high-temperature gradients in the process of heating. This information can then be used for thermal analysis for predicting the heating of nanoparticle to identify the melting or evaporation. The code is also applied to detection of defects on nanoparticles sitting on a surface. This discussion is outlined in the Appendix A.1 of the thesis.

5.2. Future Work

During this thesis, we developed a second code starting from the DDA-SI package reported by Loke and Mengüç. The present code, DDA-SI-v is vectorized and optimized to work much faster using MATLAB. The following additions are desired for the further development of the code:

- DDA-SI toolbox computational speed can be further improved by writing the package in FORTRAN or C/C+, which the new package can be more practical to use in inverse far-field scattering problems.
- Formulating DDA-SI method for a multilayered substrate or formulate the effect of two parallel substrates with nanoparticle in between.
- Using filtered coupled method [64] with surface interaction.

After these, the code can be used for study of many complex physical problems, including:

- The absorption rate and the field intensity inside a metallic nanoparticle studied in this thesis, can be used for solving the energy equation in the nano-size system for calculating the temperature rise.
- Studying the temperature rise in the AFM tip for different tip materials in the case of interaction with plasmonic geometries.
- High losses by absorption in plasmonics is a problem in the spectroscopic analysis due to temperature rise and change of optical properties of the matter. Investigate methods to decrease the absorption in the plasmonic structures.
- Analyzing the emission caused by heating the NP, and using the emission spectrum for characterization of the objects.

APPENDIX A: Defect Detection in Nanoparticles and Nano-structures

A.1. Light Scattering and Characterization

Light scattering can be used for characterization of nano-structures on surfaces, surface impurities and defect detection for nanomanufacturing applications and related industries such as semiconductor industry. Light scattering from a defected nano-size dielectric objects on a surface compared with both plane wave illumination and surface evanescent illumination and the possibility of detecting a void inside a nano-size object through scanning far-field scattering discussed in this section. The analysis can be the a base ground for inverse analysis for defect detection in nano-structures. Electromagnetic scattering by nano-size objects on a surface is a very important problem due to the fact that light scattering has proved to be one of the powerful techniques for probing various properties. Electromagnetic scattering is one of the best diagnostic tools since it can be used remotely and the intensities normally used does not affect the tested system. A number of processes can occur when light interacts with a system such as reflection, refraction, and diffraction. The combination of these is called, "scattering". Basics of light scattering by small particles can be found in [65,66]. There are some analytical solutions for light scattering by different geometries. Light scattering from a cylinder was solved analytically by Rayleigh by 1881. In 1905, Mie solved the scattering from a sphere [47]. Scattering by a small sphere near a surface is solved later on by Bobber [67]. Scattering by two parallel cylinders and a cylinder on surface solved by Yousif [68]. Light scattering problem for a sphere on or near a surface is solved by an extension of Mie theory studied by Videen [69].

The far-field scattering of objects on a surface can be calculated with DDA-SI and used in the inverse analysis for finding a possible defect inside or underneath the particle, which cannot be detected by other imaging techniques. The analysis conducted for far-field scattering can be the basis of inverse problems for detection of

the geometry of the particle or detecting the shape or location of a defect.

A.2. Defect Detection of a Cube on Semi-Infinite Surface

A.2.1. Detection of a Missing Octant

A SiO_2 cube with length of 300 nm is sitting on a Si surface as shown in Figure A.1. The incident wave is Transverse Electric (TE), polarized with wavelength of $\lambda = 632.8$ nm, with emission angle $\theta_1 = 65°$, and emission takes in a plane with an azimuthal angle of $\phi = 0°$, where θ_1 and ϕ defined in Figure A.1. The refractive index of substrate and scatterer are considered $\bar{n}_{Si} = 3.85+0.018i$ and $\bar{n}_{SiO_2} = 1.43$ respectively. Taubenblatt & Tran [29] studied the far-field scattering for this cube with a missing octant in the top left, top right and bottom right as different defect cases. Missing octant of the cube is showed in Figure A.2 according to the directions we defined relative to Cartesian coordinate system. Far-field scattering for the system calculated in the $y - z$ plane ($\phi = 0°$) for polar angle changing in the range of $-87° < \theta < 87°$. Loke and Mengüç reproduced identical results with DDA-SI [32]. The results also reproduced in this thesis, as represented in Figure A.3. In the plot, r_{det} is the distance in which the far-field scattering is calculated and $k = 2\pi/n_{bulk}$, which here the bulk medium is considered air ($n_{bulk} = 1$). In all the analysis far field intensities normalized with incident wave amplitude.

The interaction of the scatterer with the surface evanescent wave was also compared with reproduced results. This approach is showed in Figure A.4, where a TE polarized wave is incident from the back of the substrate with incident angle $\theta_1 = 20°$, where θ_1 is greater than the critical angle of emission in respect to refractive indices of Si and air. There will be TIR and a surface evanescent wave on the surface, with an incident wave in the $y - z$ plane ($\phi = 0°$). The far-field scattering is calculated in $y - z$ plane with $-87° < \theta < 87°$ as shown in Figure A.5. comparing Figures A.3 and A.5, using evanescent illumination result in a far-field scattering pattern that is more detectable due to the shift in the extremum in each missing notch case. Use of evanescent wave can also be beneficial when the defect is underneath the scatterer.

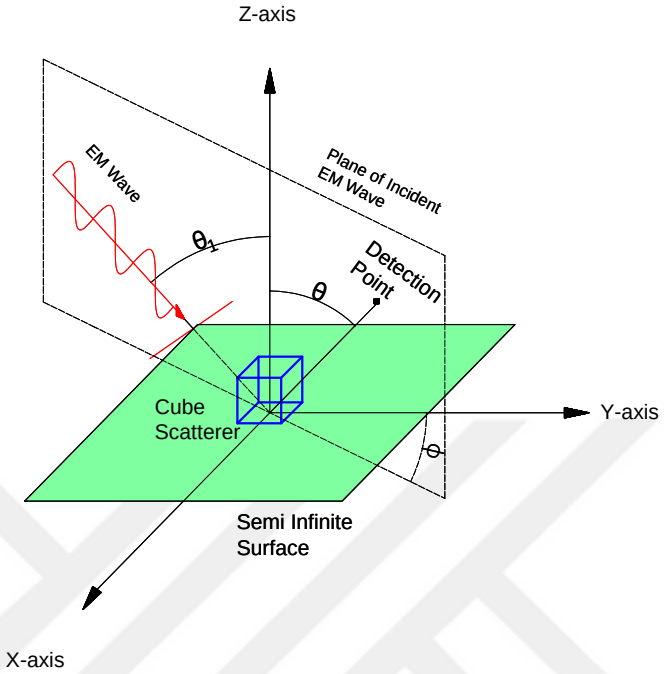

Figure A.1: SiO_2 on Si surface under plan wave illumination.

In this case, the change in the far-field scattering under plane wave illumination with comparison with non-defected scatterer is very slight. However, a surface wave in the case illuminated in a correct direction can make a significant difference in far-field scattering between the defected and non-defected cases.

A.2.2. Effect of Void Inside the Cube under Evanescent Illumination

In the case that a defect is internal and detection with other direct imaging techniques is not possible, scattering can be considered. A void inside the nanoparticle or a piece of a material different than the material of the nanoparticle can be considered as an internal defect. The same configuration, mentioned in Section A.2.1 under evanescent illumination as Figure A.4 with $\theta_1 = 20°$ and $\phi = 0°$, is analysed. However, there is spherical void in the center of SiO_2 cube as a defect. We calculate this configuration for two different void diameter of 150 nm and 225 nm and compared it to

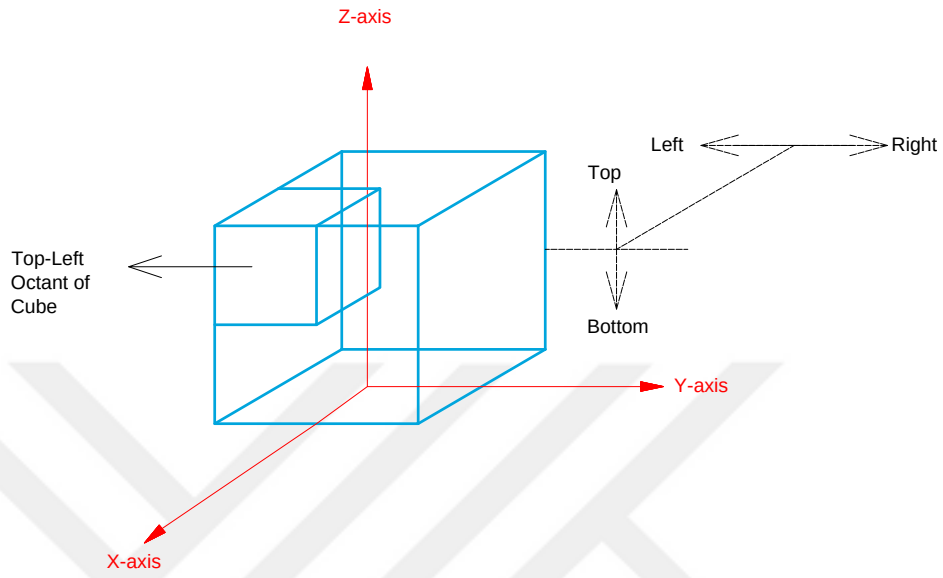

Figure A.2: Defining the position of an octant of a cube.

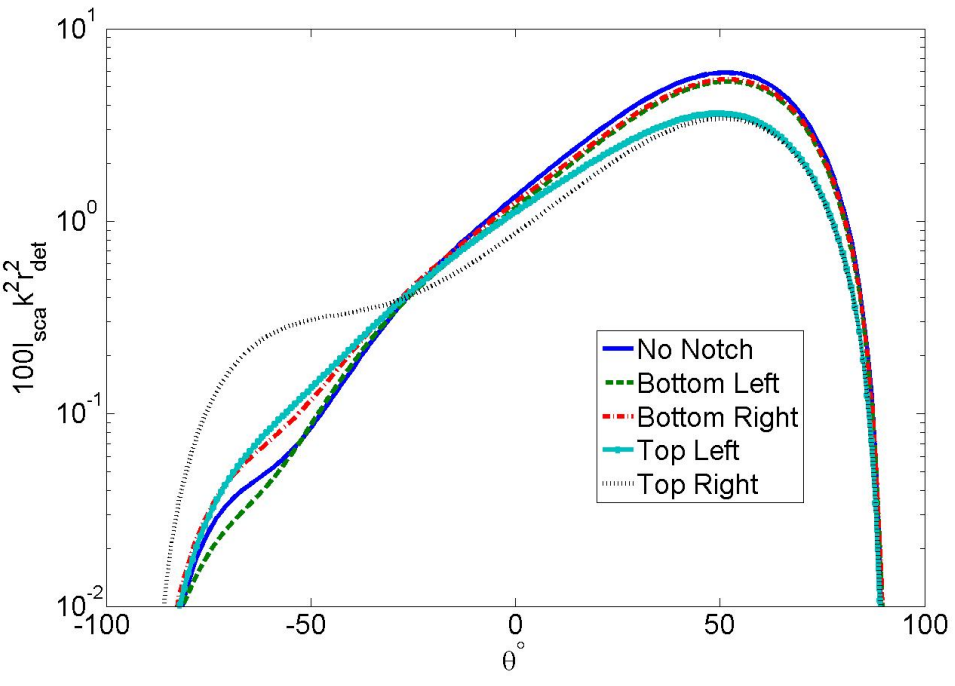

Figure A.3: SiO_2 on Si surface under plan wave illumination.

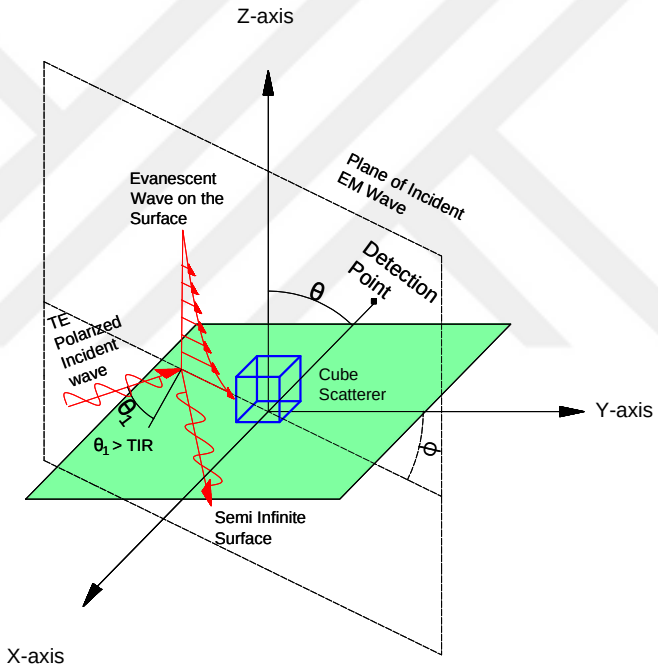

Figure A.4: SiO_2 on Si surface under evanescent wave illumination.

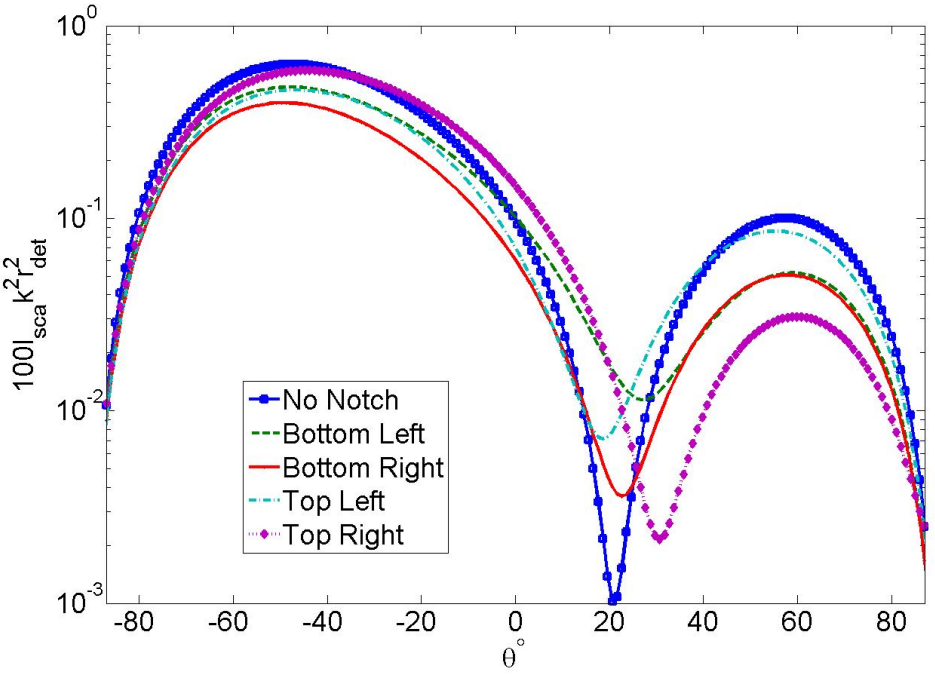

Figure A.5: Far-field scattering from a SiO_2 cube on Si surface under surface evanescent wave illumination.

the non-voided cube scatterer. Far-field scattering is calculated in two different planes, the $y-z$ plane where $\phi = 0°$ indicated with "s" subscript in the figure, and the $x-z$ plane where $\phi = 90°$ indicated with "p" subscript in the Figure A.6. The polar angle of detection is changing in the $-87° < \theta < 87°$ range. In the case of the cube without any void 6859 dipoles are used to represent the cube. The results are shown in Figure A.6. From the results in regards to $x-z$ plane, between the angles $-58° < \theta < 58°$, a change in the concavity of far-field scattering is observable. The concavity in the non-voided case is negative and by increasing the void size, it shifts to positive. Defect detection with using $x-z$ plane data will be challenging as the presence of the void does not shift the extremum of the phase function. However, there exist a shift between the scattering angles of $10° < \theta < 25°$ in far-field scattering in $y-z$ plane. As void size increases, the minimum of the phase function shifts to backward angles.

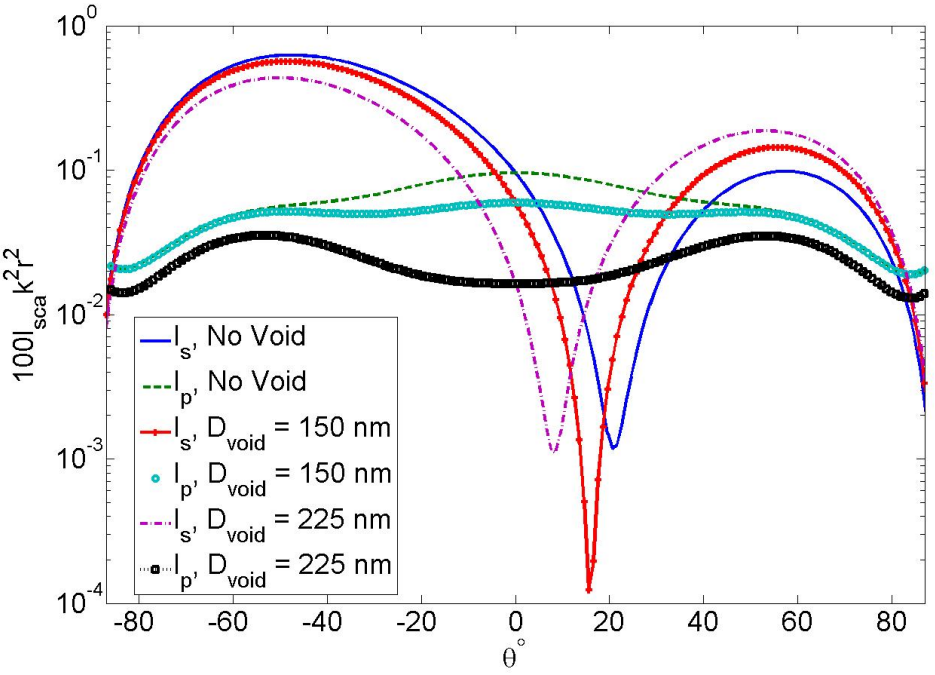

Figure A.6: Far-field scattering from a SiO_2 cube on Si surface under surface evanescent wave illumination with/without a spherical void inside.

A.3. Detection of a Missing NP in a Chain of Spherical NP

A.3.1. Plane Wave Illumination with Different Angles of Incidence

An array of 300 nm in diameter SiO_2 nano-spheres are sitting on a semi-infinite Si substrate with center to center spacing of 320 nm between the NPs. The system is initially analysed with a plane wave illumination as shown in Figure A.7. For plane wave illumination we analysed the far-field scattering of the system with a missing nano-sphere for two different angles of incidence $\theta_1 = -30°$ and $\theta_1 = -70°$. The azimuthal angle of the incident plane is $\phi = 0°$. The nano-spheres are aligned in the $y - axis$ direction and incident wave has TE polarization (E-field is in the $x - axis$ direction). Results for the scattering of the system with $\theta_1 = -30°$ incident angle of illumination in $y - z$ plane (Azimuthal angle is $\phi = 0°$) is shown in Figure A.8. With the same illumination angle for scattering captured in $x - z$ plane (Azimuthal angle is $\phi = 90°$), and the results are shown in Figure A.9. The same analysis was carried out

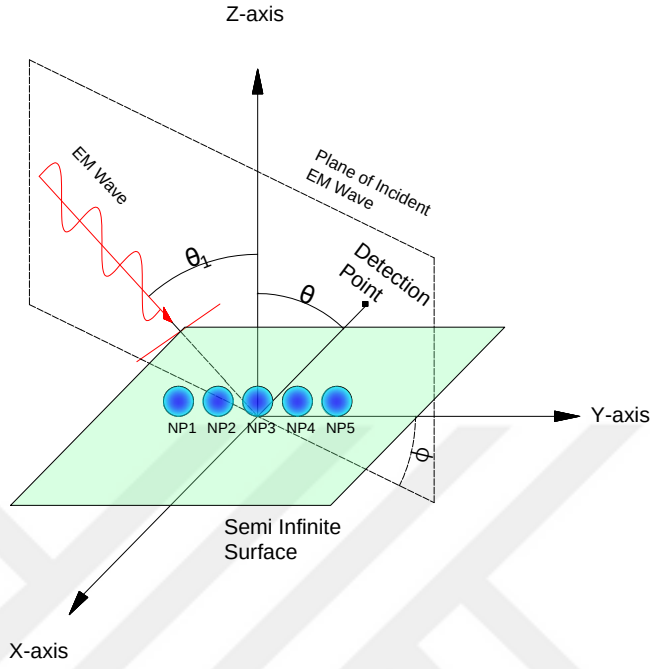

Figure A.7: Spherical SiO_2 NPs sitting on a Si substrate under TE plane wave illumination.

with $\theta_1 = -70°$ incident angle of TE-polarized plane wave illumination. For far-field scattering captured in $y-z$ plane (Azimuthal angle is $\phi = 0°$) the results are shown in Figure A.10 and for scattering in $x-z$ plane (Azimuthal angle is $\phi = 90°$) the results are shown in Figure A.11.

A.3.2. Under Evanescent Illumination

The same system described in Section A.3.1 is analysed with surface decaying evanescent wave. The incident radiation is from the back of the substrate with $\theta_1 = 20°$ polar and $\phi = 0°$ azimuthal angle of incidents resulted in TIR. Consequently the direction of the K-vector will be to positive $y-$direction decaying in the $z-$direction and symmetrical E-field shape in $x - axis$. The system initially analysed for the configuration which NPs are aligned in the $y-$ direction. The schematic view of the

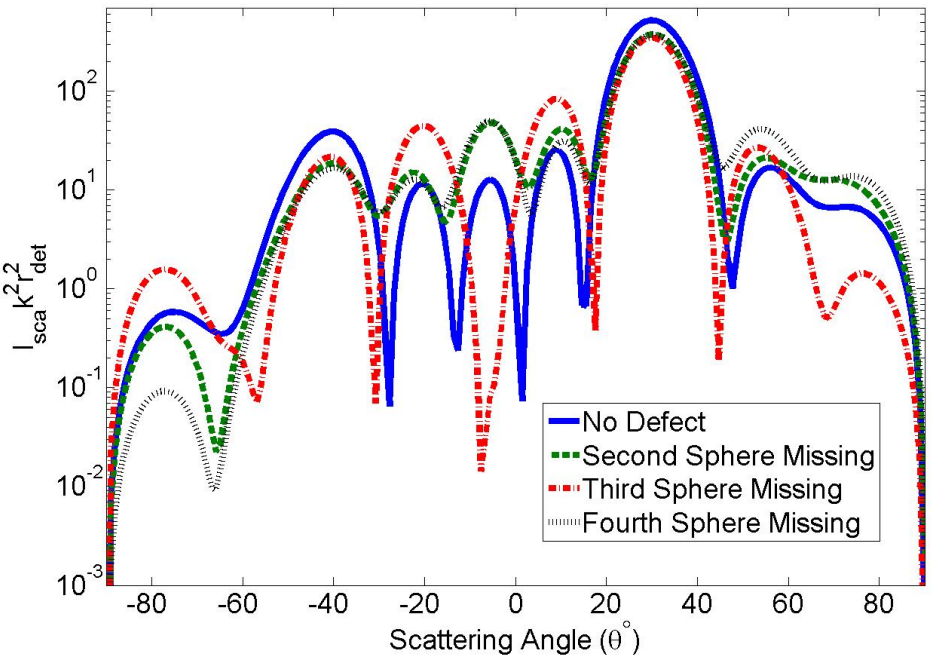

Figure A.8: Far-field scattering of a row of SiO_2 under plane wave illumination with incident angle of $\theta_1 = 30°$. Far-field scattering is measured with azimuthal angle $\phi = 0°$ $(yz - palne)$ with polar angle with interval of $-90° < \theta < 90°$.

.

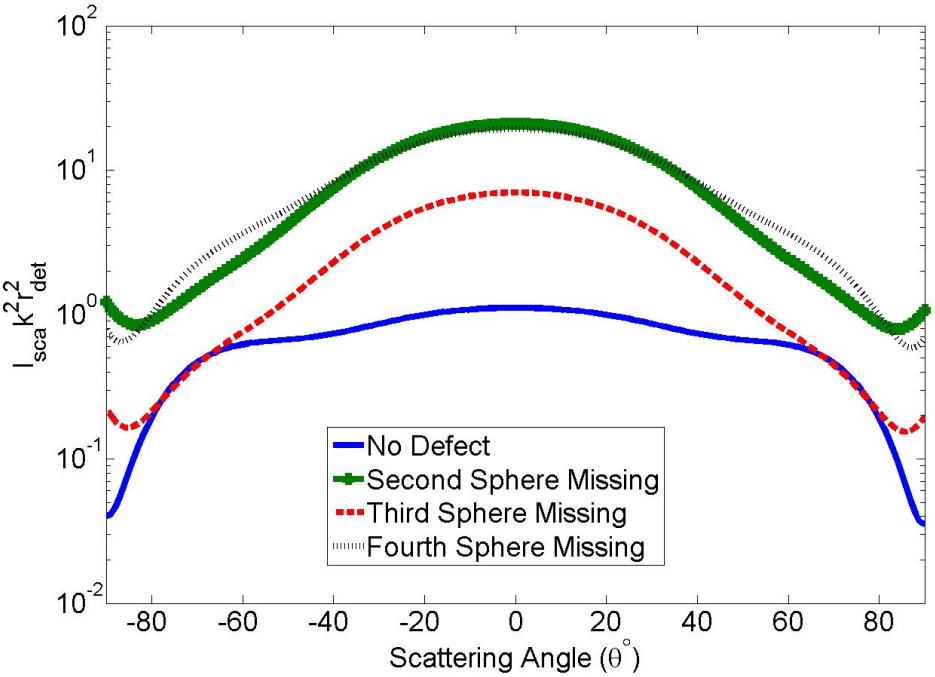

Figure A.9: Far-field scattering of a row of SiO_2 under plane wave illumination with incident angle of $\theta_1 = 30°$. Far-field scattering is measured with azimuthal angle $\phi = 90°$ $(xz - palne)$ with polar angle with interval of $-90° < \theta < 90°$.

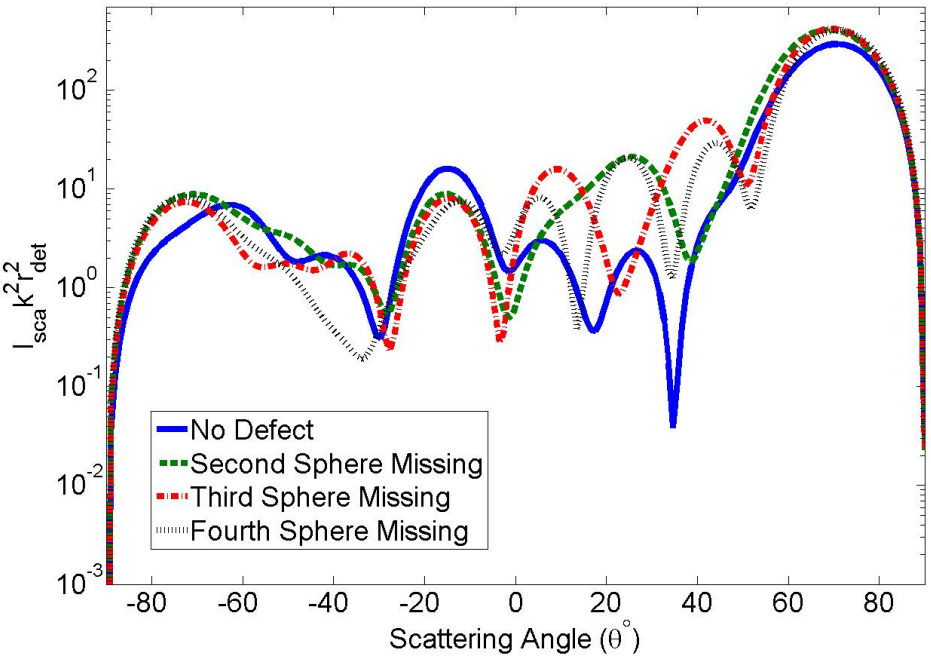

Figure A.10: Far-field scattering of a row of SiO_2 under plane wave illumination with incident angle of $\theta_1 = 70°$. Far-field scattering is measured with azimuthal angle $\phi = 90°$ $(xz - palne)$ with polar angle with interval of $-90° < \theta < 90°$.

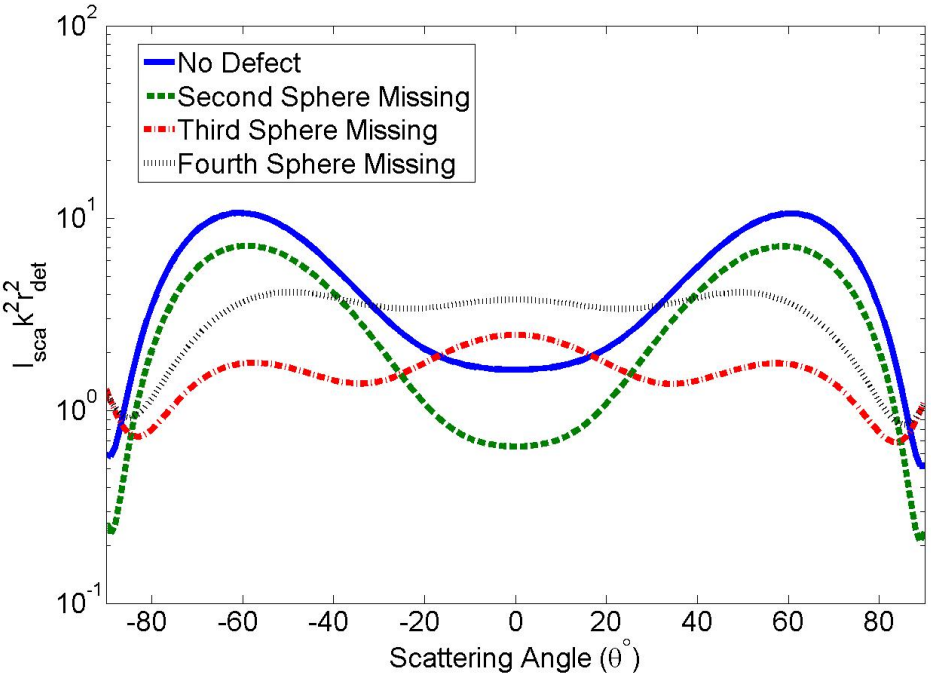

Figure A.11: Far-field scattering of a row of SiO_2 under plane wave illumination with incident angle of $\theta_1 = 70°$. Far-field scattering is measured with azimuthal angle $\phi = 90°$ $(xz - palne)$ with polar angle with interval of $-90° < \theta < 90°$.

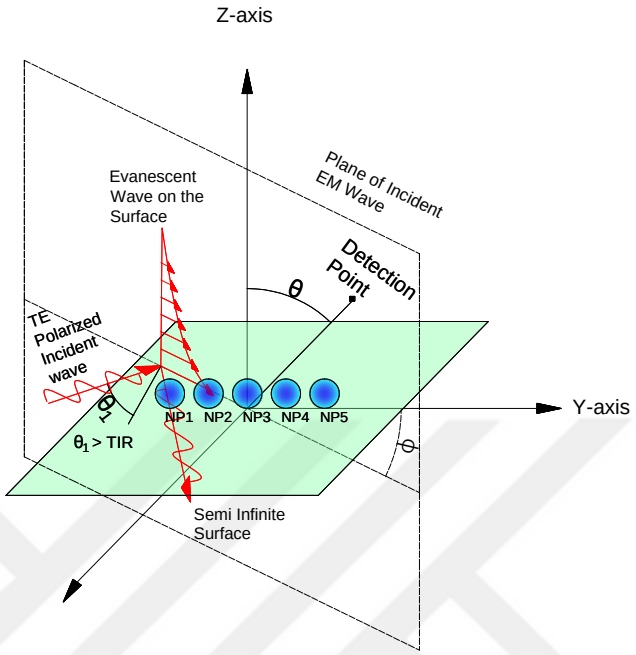

Figure A.12: Spherical SiO_2 NPs sitting on a Si substrate under decaying evanescent surface wave.

system can be seen in Figure A.12. The far-field scattering calculated in $y-z$ plane and $x-z$ plane, where the azimuthal angle of far-field scattering will be $\phi = 0°$ and $\phi = 90°$, respectively. The results can be seen in Figures A.13 and A.14. From the results we can observe that row of spheres aligned along $y-axis$ and K-vector of surface wave in $x-$direction, detection of missing NP can be easier with capturing the far-field scattering in $y-z$ plane. In the case of spherical NPs aligned in the $x-$direction, as represented in Figure A.15, the results are computed in two different planes of $\phi = 0°$ and $\phi = 90°$ azimuthal angles. The results are presented in Figure A.16 and A.17. By comparison of two plots we can conclude that in the case of a fixed K-vector and NPs aligned in $x-axis$, detection of a missing NP can be easier with looking at far-field scattering in plane with $\phi = 0°$ azimuthal angle.

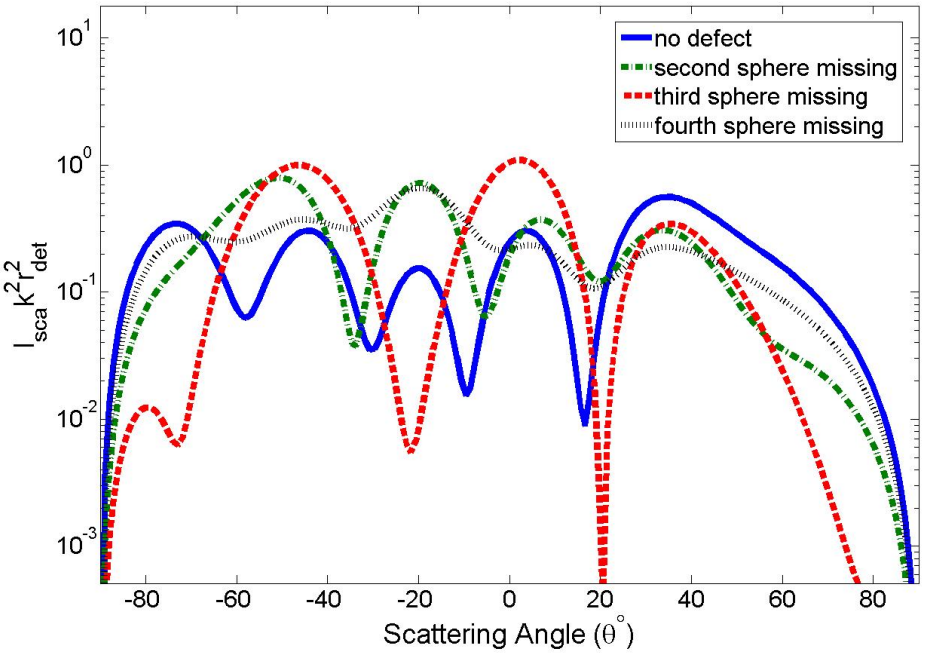

Figure A.13: Spherical SiO_2 NPs sitting on a Si substrate under decaying evanescent surface wave.

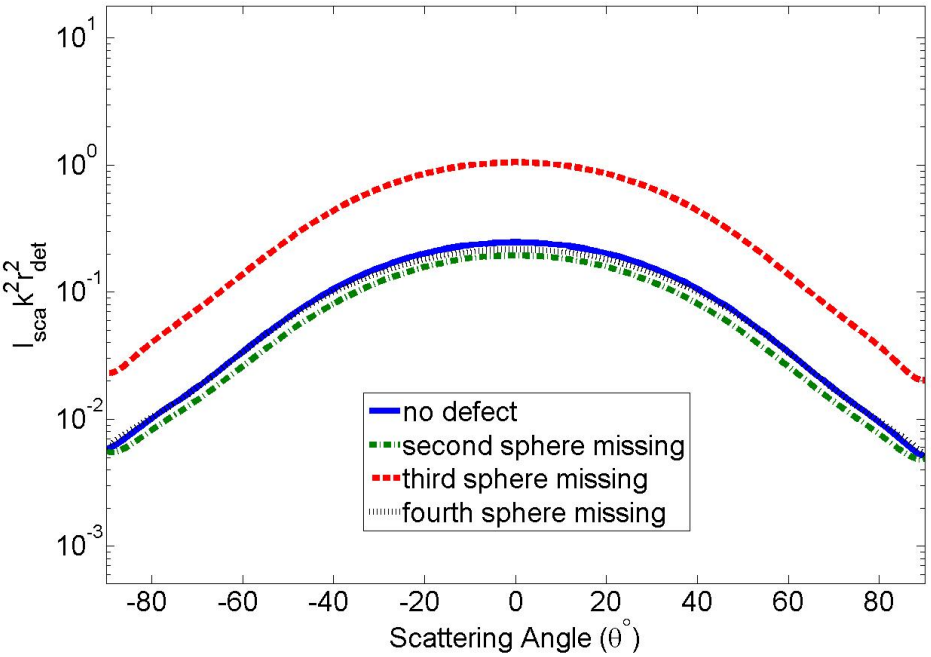

Figure A.14: Spherical SiO_2 NPs sitting on a Si substrate under decaying evanescent surface wave.

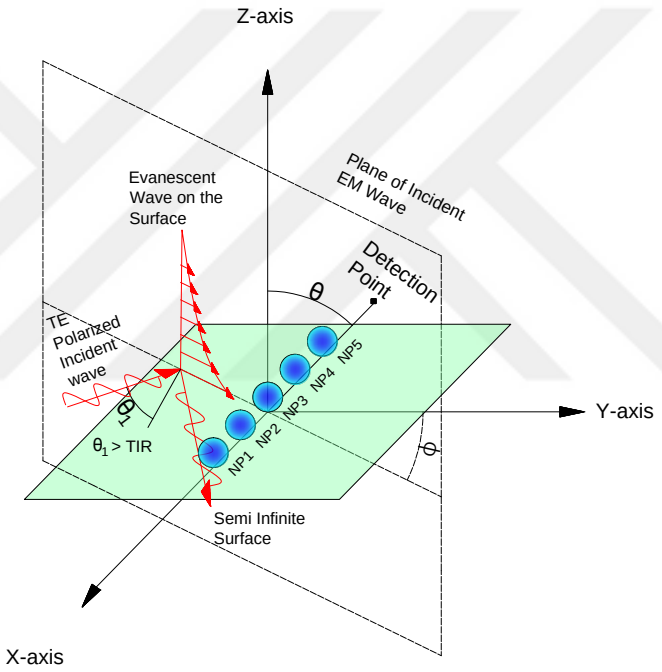

Figure A.15: Spherical SiO_2 NPs sitting on a Si substrate under decaying evanescent surface wave.

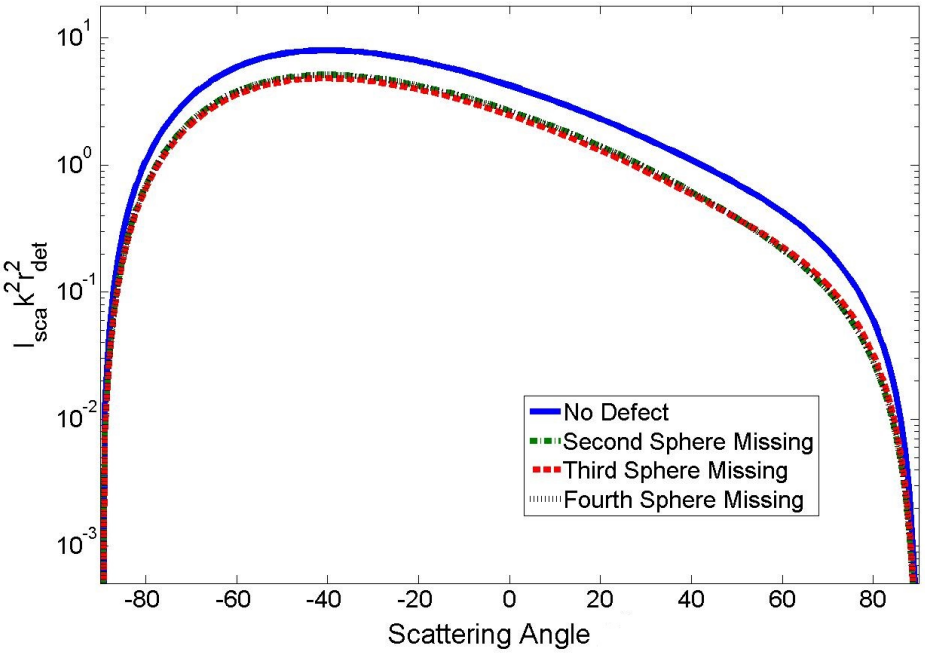

Figure A.16: Spherical SiO_2 NPs sitting on a Si substrate under decaying evanescent surface wave.

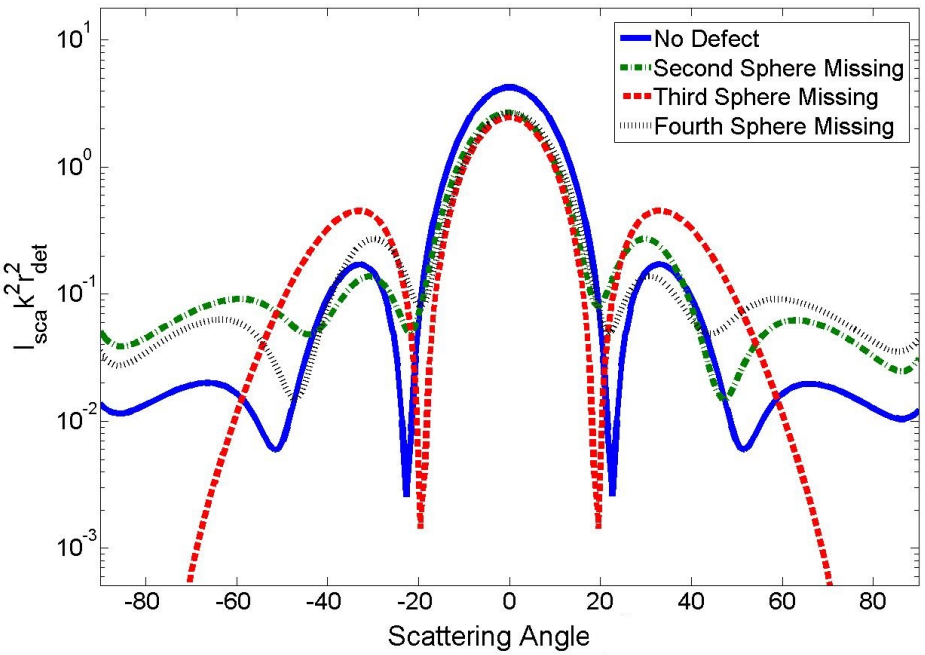

Figure A.17: Spherical SiO_2 NPs sitting on a Si substrate under decaying evanescent surface wave.

REFERENCES

1. Zhang, Z. M., *Nano/microscale heat transfer*, McGraw-Hill New York, 2007.

2. Chen, G., "Nanoscale energy transport and conversion", , 2005.

3. Moniz, E. J. and J. García-Martínez, *Nanotechnology for the energy challenge*, John Wiley & Sons, 2010.

4. Huang, X., I. H. El-Sayed, W. Qian and M. A. El-Sayed, "Cancer cell imaging and photothermal therapy in the near-infrared region by using gold nanorods", *Journal of the American Chemical Society*, Vol. 128, No. 6, pp. 2115–2120, 2006.

5. Neely, A., C. Perry, B. Varisli, A. K. Singh, T. Arbneshi, D. Senapati, J. R. Kalluri and P. C. Ray, "Ultrasensitive and highly selective detection of Alzheimer's disease biomarker using two-photon Rayleigh scattering properties of gold nanoparticle", *Acs Nano*, Vol. 3, No. 9, pp. 2834–2840, 2009.

6. Lee, H., E. Sun, D. Ham and R. Weissleder, "Chip–NMR biosensor for detection and molecular analysis of cells", *Nature medicine*, Vol. 14, No. 8, pp. 869–874, 2008.

7. Ahmed, W. and M. J. Jackson, *Emerging nanotechnologies for manufacturing*, William Andrew, 2014.

8. Amendola, V., O. M. Bakr and F. Stellacci, "A study of the surface plasmon resonance of silver nanoparticles by the discrete dipole approximation method: effect of shape, size, structure, and assembly", *Plasmonics*, Vol. 5, No. 1, pp. 85–97, 2010.

9. Alabastri, A., S. Tuccio, A. Giugni, A. Toma, C. Liberale, G. Das, F. D. Angelis, E. D. Fabrizio and R. P. Zaccaria, "Molding of plasmonic resonances in metallic

nanostructures: Dependence of the non-linear electric permittivity on system size and temperature", *Materials*, Vol. 6, No. 11, pp. 4879–4910, 2013.

10. Rodríguez-Oliveros, R., J. A. Sánchez-Gil *et al.*, "Localized surface-plasmon resonances on single and coupled nanoparticles through surface integral equations for flexible surfaces", *Optics express*, Vol. 19, No. 13, pp. 12208–12219, 2011.

11. Funston, A. M., C. Novo, T. J. Davis and P. Mulvaney, "Plasmon coupling of gold nanorods at short distances and in different geometries", *Nano letters*, Vol. 9, No. 4, pp. 1651–1658, 2009.

12. Loke, V., G. Huda, E. Donev, V. Schmidt, J. Hastings, M. P. Mengüç and T. Wriedt, "Comparison between discrete dipole approximation and other modelling methods for the plasmonic response of gold nanospheres", *Applied Physics B*, Vol. 115, No. 2, pp. 237–246, 2014.

13. Maier, S. A., *Plasmonics: fundamentals and applications*, Springer Science & Business Media, 2007.

14. Stockman, M. I., "Nanoplasmonics: past, present, and glimpse into future", *Optics express*, Vol. 19, No. 22, pp. 22029–22106, 2011.

15. Bharadwaj, P., B. Deutsch and L. Novotny, "Optical antennas", *Advances in Optics and Photonics*, Vol. 1, No. 3, pp. 438–483, 2009.

16. Hawes, E., J. Hastings, C. Crofcheck and M. Mengüç, "Spatially selective melting and evaporation of nanosized gold particles", *Optics letters*, Vol. 33, No. 12, pp. 1383–1385, 2008.

17. McCarthy, B., Y. Zhao, R. Grover and D. Sarid, "Enhanced Raman scattering for temperature measurement of a laser-heated atomic force microscope tip", *Applied Physics Letters*, Vol. 86, No. 11, p. 111914, 2005.

18. Madrazo, A. and M. Nieto-Vesperinas, "Reconstruction of corrugated dielectric surfaces with a model of a photon scanning tunneling microscope: influence of the tip on the near field", *JOSA A*, Vol. 14, No. 3, pp. 618–628, 1997.

19. Joulain, K., P. Ben-Abdallah, P.-O. Chapuis, Y. De Wilde, A. Babuty and C. Henkel, "Strong tip–sample coupling in thermal radiation scanning tunneling microscopy", *Journal of Quantitative Spectroscopy and Radiative Transfer*, Vol. 136, pp. 1–15, 2014.

20. Caldarola, M., P. Albella, E. Cortés, M. Rahmani, T. Roschuk, G. Grinblat, R. F. Oulton, A. V. Bragas and S. A. Maier, "Non-plasmonic nanoantennas for surface enhanced spectroscopies with ultra-low heat conversion", *Nature communications*, Vol. 6, 2015.

21. Albella, P., R. Alcaraz de la Osa, F. Moreno and S. A. Maier, "Electric and magnetic field enhancement with ultralow heat radiation dielectric nanoantennas: Considerations for surface-enhanced spectroscopies", *ACS Photonics*, Vol. 1, No. 6, pp. 524–529, 2014.

22. Alonso-González, P., P. Albella, M. Schnell, J. Chen, F. Huth, A. García-Etxarri, F. Casanova, F. Golmar, L. Arzubiaga, L. Hueso *et al.*, "Resolving the electromagnetic mechanism of surface-enhanced light scattering at single hot spots", *Nature communications*, Vol. 3, p. 684, 2012.

23. DeVoe, H., "Optical properties of molecular aggregates. I. Classical model of electronic absorption and refraction", *The Journal of chemical physics*, Vol. 41, No. 2, pp. 393–400, 1964.

24. Purcell, E. M. and C. R. Pennypacker, "Scattering and absorption of light by nonspherical dielectric grains", *The Astrophysical Journal*, Vol. 186, pp. 705–714, 1973.

25. Draine, B. T. and P. J. Flatau, "Discrete-dipole approximation for scattering calcu-

lations", *Journal of the Optical Society of America A*, Vol. 11, No. 4, pp. 1491–1499, apr 1994.

26. Draine, B. T. and P. J. Flatau, "Discrete-dipole approximation for periodic targets: theory and tests", *JOSA A*, Vol. 25, No. 11, pp. 2693–2703, 2008.

27. Yurkin, M. A., M. Min and A. G. Hoekstra, "Application of the discrete dipole approximation to very large refractive indices: Filtered coupled dipoles revived", *Physical Review E*, Vol. 82, No. 3, p. 036703, 2010.

28. Yurkin, M. A. and A. G. Hoekstra, "The discrete-dipole-approximation code ADDA: capabilities and known limitations", *Journal of Quantitative Spectroscopy and Radiative Transfer*, Vol. 112, No. 13, pp. 2234–2247, 2011.

29. Taubenblatt, M. A. and T. K. Tran, "Calculation of light scattering from particles and structures on a surface by the coupled-dipole method", *JOSA A*, Vol. 10, No. 5, pp. 912–919, 1993.

30. Schmehl, R., B. M. Nebeker, E. D. Hirleman *et al.*, "Discrete-dipole approximation for scattering by features on surfaces by means of a two-dimensional fast Fourier transform technique", *JOSA A*, Vol. 14, No. 11, pp. 3026–3036, 1997.

31. Nebeker, B. M., "Modeling of light scattering from features above and below surfaces using the discrete-dipole approximation", , 1998.

32. Loke, V. L., M. P. Mengüç and T. A. Nieminen, "Discrete-dipole approximation with surface interaction: Computational toolbox for MATLAB", *Journal of Quantitative Spectroscopy and Radiative Transfer*, Vol. 112, No. 11, pp. 1711–1725, jul 2011.

33. Waxenegger, J., A. Trügler and U. Hohenester, "Plasmonics simulations with the MNPBEM toolbox: Consideration of substrates and layer structures", *Computer Physics Communications*, Vol. 193, pp. 138–150, 2015.

34. Short, M. R., J.-M. Geffrin, R. Vaillon, H. Tortel, B. Lacroix and M. Francoeur, "Evanescent wave scattering by particles on a surface: Validation of the discrete dipole approximation with surface interaction against microwave analog experiments", *Journal of Quantitative Spectroscopy and Radiative Transfer*, Vol. 146, pp. 452–458, 2014.

35. Huda, G. M., E. U. Donev, M. P. Mengüç and J. T. Hastings, "Effects of a silicon probe on gold nanoparticles on glass under evanescent illumination", *Optics express*, Vol. 19, No. 13, pp. 12679–12687, 2011.

36. Huda, G. M., M. P. Mengüç and J. T. Hastings, "Absorption suppression of silver nanoparticles in the presence of an AFM tip: A harmonic oscillator model", *THE FIFTH INTERNATIONAL WORKSHOP ON THEORETICAL AND COMPUTATIONAL NANO-PHOTONICS: TaCoNa-Photonics 2012*, Vol. 1475, pp. 134–136, AIP Publishing, 2012.

37. Huda, G. M. and J. Hastings, "Absorption Modulation of Plasmon Resonant Nanoparticles in the Presence of an AFM Tip", *Selected Topics in Quantum Electronics, IEEE Journal of*, Vol. 19, No. 3, pp. 4602306–4602306, 2013.

38. Loke, V. L. and M. P. Mengüç, "Surface waves and atomic force microscope probe-particle near-field coupling: discrete dipole approximation with surface interaction", *JOSA A*, Vol. 27, No. 10, pp. 2293–2303, 2010.

39. Francoeur, M. and M. P. Mengüç, "Role of fluctuational electrodynamics in near-field radiative heat transfer", *Journal of Quantitative Spectroscopy and Radiative Transfer*, Vol. 109, No. 2, pp. 280–293, 2008.

40. Didari, A. and M. P. Mengüç, "Analysis of near-field radiation transfer within nanogaps using FDTD method", *Journal of Quantitative Spectroscopy and Radiative Transfer*, Vol. 146, pp. 214–226, 2014.

41. Didari, A. and M. P. Mengüç, "Near-to far-field coherent thermal emission by

surfaces coated by nanoparticles and the evaluation of effective medium theory", *Optics Express*, Vol. 23, No. 11, pp. A547–A552, 2015.

42. Didari, A. and M. P. Mengüç, "Near-field thermal emission between corrugated surfaces separated by nano-gaps", *Journal of Quantitative Spectroscopy and Radiative Transfer*, Vol. 158, pp. 43–51, 2015.

43. Edalatpour, S. and M. Francoeur, "The Thermal Discrete Dipole Approximation (T-DDA) for near-field radiative heat transfer simulations in three-dimensional arbitrary geometries", *Journal of Quantitative Spectroscopy and Radiative Transfer*, Vol. 133, pp. 364–373, 2014.

44. Jackson, J. D. and J. D. Jackson, *Classical electrodynamics*, Vol. 3, Wiley New York etc., 1962.

45. Schwinger, J. S., W. Tsai, L. L. De Raad and K. Milton, *Classical electrodynamics*, Perseus, 1998.

46. Hehl, F. W. and Y. N. Obukhov, *Foundations of classical electrodynamics: Charge, flux, and metric*, Vol. 33, Springer Science & Business Media, 2012.

47. Mie, G., "Beiträge zur Optik trüber Medien, speziell kolloidaler Metallösungen", *Annalen der physik*, Vol. 330, No. 3, pp. 377–445, 1908.

48. Taflove, A. and S. C. Hagness, *Computational electrodynamics*, Artech house, 2005.

49. Banerjee, P. K. and R. Butterfield, *Boundary element methods in engineering science*, Vol. 17, McGraw-Hill London, 1981.

50. Hohenester, U. and A. Trügler, "MNPBEM–A Matlab toolbox for the simulation of plasmonic nanoparticles", *Computer Physics Communications*, Vol. 183, No. 2, pp. 370–381, 2012.

51. Hohenester, U., "Simulating electron energy loss spectroscopy with the MNPBEM

toolbox", *Computer Physics Communications*, Vol. 185, No. 3, pp. 1177–1187, 2014.

52. Sullivan, D. M., *Electromagnetic simulation using the FDTD method*, John Wiley & Sons, 2013.

53. Oskooi, A. F., D. Roundy, M. Ibanescu, P. Bermel, J. Joannopoulos and S. G. Johnson, "MEEP: A flexible free-software package for electromagnetic simulations by the FDTD method", *Computer Physics Communications*, Vol. 181, No. 3, pp. 687–702, 2010.

54. Didari, A. and M. P. Mengüç, "Near-field thermal radiation transfer by mesoporous metamaterials", *Optics Express*, Vol. 23, No. 19, pp. A1253–A1258, 2015.

55. Jin, J.-M., *The finite element method in electromagnetics*, John Wiley & Sons, 2014.

56. Waterman, P., "Matrix formulation of electromagnetic scattering", *Proceedings of the IEEE*, Vol. 53, No. 8, pp. 805–812, 1965.

57. Loke, V. L., E. U. Donev, G. M. Huda, J. T. Hastings, M. P. Mengüç and T. Wriedt, "Discrete dipole aproximation of gold nanospheres on substrates: Considerations and comparision with other discretization methods", *AAPP— Physical, Mathematical, and Natural Sciences*, Vol. 89, No. S1, 2011.

58. Johnson, P. B. and R.-W. Christy, "Optical constants of the noble metals", *Physical Review B*, Vol. 6, No. 12, p. 4370, 1972.

59. Tojo, S. and M. Hasuo, "Oscillator-strength enhancement of electric-dipole-forbidden transitions in evanescent light at total reflection", *Physical Review A*, Vol. 71, No. 1, p. 012508, 2005.

60. Palik, E., "Handbook of Optical Constants of Solids, Volumes I, II, and III: Subject

Index and Contributor Index", *Palik, ed.(Elsevier Science & Tech, 1985)*, p. 804, 1985.

61. Pattani, V. P. and J. W. Tunnell, "Nanoparticle-mediated photothermal therapy: A comparative study of heating for different particle types", *Lasers in surgery and medicine*, Vol. 44, No. 8, pp. 675–684, 2012.

62. Honda, M., Y. Saito, N. I. Smith, K. Fujita and S. Kawata, "Nanoscale heating of laser irradiated single gold nanoparticles in liquid", *Optics express*, Vol. 19, No. 13, pp. 12375–12383, 2011.

63. Grigoriev, V., N. Bonod, J. Wenger and B. Stout, "Optimizing nanoparticle designs for ideal absorption of light", *ACS Photonics*, Vol. 2, No. 2, pp. 263–270, 2015.

64. Piller, N. B. and O. J. Martin, "Increasing the performance of the coupled-dipole approximation: A spectral approach", *Antennas and Propagation, IEEE Transactions on*, Vol. 46, No. 8, pp. 1126–1137, 1998.

65. Bohren, C. F. and D. R. Huffman, *Absorption and scattering of light by small particles*, John Wiley & Sons, 2008.

66. Mishchenko, M. I., L. D. Travis and A. A. Lacis, *Scattering, absorption, and emission of light by small particles*, Cambridge university press, 2002.

67. Bobbert, P. and J. Vlieger, "Light scattering by a sphere on a substrate", *Physica A: Statistical Mechanics and its Applications*, Vol. 137, No. 1, pp. 209–242, 1986.

68. Yousif, H., *Light scattering from parallel tilted fibers*, Ph.D. Thesis, Ph. D. dissertation (Department of Physics, University of Arizona, Tucson, Ariz., 1987), 1987.

69. Videen, G., "Light scattering from a sphere on or near a surface", *JOSA A*, Vol. 8, No. 3, pp. 483–489, 1991.